Tectonics

A statistical assessment of seismic models of the U.S. continental crust using Bayesian inversion of ambient noise surface wave dispersion data

T. M. Olugboji[1] (ID)**, V. Lekic[1]** (ID)**, and W. McDonough[1]** (ID)

[1]Department of Geology, University of Maryland, College Park, Maryland, USA

Abstract We present a new approach for evaluating existing crustal models using ambient noise data sets and its associated uncertainties. We use a transdimensional hierarchical Bayesian inversion approach to invert ambient noise surface wave phase dispersion maps for Love and Rayleigh waves using measurements obtained from Ekström (2014). Spatiospectral analysis shows that our results are comparable to a linear least squares inverse approach (except at higher harmonic degrees), but the procedure has additional advantages: (1) it yields an autoadaptive parameterization that follows Earth structure without making restricting assumptions on model resolution (regularization or damping) and data errors; (2) it can recover non-Gaussian phase velocity probability distributions while quantifying the sources of uncertainties in the data measurements and modeling procedure; and (3) it enables statistical assessments of different crustal models (e.g., CRUST1.0, LITHO1.0, and NACr14) using variable resolution residual and standard deviation maps estimated from the ensemble. These assessments show that in the stable old crust of the Archean, the misfits are statistically negligible, requiring no significant update to crustal models from the ambient noise data set. In other regions of the U.S., significant updates to regionalization and crustal structure are expected especially in the shallow sedimentary basins and the tectonically active regions, where the differences between model predictions and data are statistically significant.

1. Introduction

Seismological models of the crust are useful for making geological inference, for instance, when combined with other geophysical and geochemical constraints; they provide our best insight into the structure and composition of Earth's continental crust [e.g., *Christensen and Mooney*, 1995; *Hans Wedepohl*, 1995; *Huang et al.*, 2013; *Rudnick and Gao*, 2014]. The most widely used models are constrained by active source data set of seismic reflection and refraction experiments and in a few cases receiver functions [e.g., *Mooney et al.*, 1998; *Laske et al.*, 2012]. For this reason the models only sparsely sample the surface of the Earth and often impose limiting assumptions by extrapolations based on tectonic regionalization. Additionally, these models do not come with estimated uncertainties, making inferences hard to evaluate. We address these two concerns for the conterminous United States where comprehensive seismic instrumentation is provided by EarthScope's USArray [e.g., *Long et al.*, 2014]. We use the extensive data sets of short-period, ambient noise phase velocity measurements for Love and Rayleigh surface waves.

Previous ambient noise seismic experiments included regional studies in both the western and eastern U.S. [*Shapiro*, 2005; *Moschetti et al.*, 2007; *Liang and Langston*, 2008; *Stachnik et al.*, 2008; *Ekström et al.*, 2009] as well as continent-wide studies [*Bensen et al.*, 2008; *Ekström*, 2014]. Together, these data sets provide an unprecedented opportunity to constrain the elastic properties of the crust and upper mantle across the conterminous United States [e.g., *Yang et al.*, 2008, 2011; *Bensen et al.*, 2009; *Moschetti et al.*, 2010a; *Shen et al.*, 2013]. Despite the proliferation of measurements, neither regional models of the U.S. crust, e.g., NACr14 [*Tesauro et al.*, 2014] nor global models like Crust5.1 [*Nataf and Ricard*, 1996; *Mooney et al.*, 1998], and its successors: Crust2.0 [*Bassin et al.*, 2000], Crust1.0 [*Laske et al.*, 2012], and LITHOS 1.0 [e.g., *Pasyanos et al.*, 2014], incorporate ambient noise, passive source data sets into their inversions.

In this study, we use ambient noise data to evaluate crustal structure and its associated uncertainties. In doing so, we apply transdimensional hierarchical Bayesian inversion (THBI) [e.g., *Bodin and Sambridge*, 2009; *Bodin et al.*, 2012b] to invert for a solution ensemble of phase velocity dispersion maps and the

optimal parameterization for these maps. The Bayesian inverse approach estimates the model uncertainties from a large sample of the posterior distribution generated by a reversible jump Markov Chain Monte Carlo (rj-McMC) sampler. By extending the Bayesian approach to the problem of estimating the model parameterization itself, we can invert for phase velocity maps without needing to make explicit, restricting assumptions on the model resolution or regularization (smoothing or damping) as required by traditional, linear, least squares inverse approaches [e.g., *Bensen et al.*, 2008; *Ekström*, 2014]. This allows us to recover, with greater confidence, fine-scale features in various sedimentary and rift basins, as well as across orogenic zones within the crust of the U.S. Accurate reconstructions of the crustal velocities in these different tectonic provinces are important for interpretation of the tectonic history and evolution of basins and orogens [e.g., *Benoit et al.*, 2014; *Pollitz and Mooney*, 2014; *Schmandt et al.*, 2015; *Zhang et al.*, 2016; *Hopper et al.*, 2017]. Additionally, they are important for making geophysical inferences about variations of crustal composition across tectonic settings, with depth, and with age [e.g., *Rudnick and Gao*, 2014; *Yuan*, 2015].

Additionally, we estimate the aggregate uncertainty ("hierarchical" parameters) that arises from both the phase dispersion measurements and from errors introduced by simplifying assumption of great circle paths in forward modeling [*Young et al.*, 2013]. We quantify the similarities and differences between maps obtained by the standard, least squares versus the THBI inversions using a multiple taper, spherical Slepian approach [e.g., *Simons et al.*, 2006]. Uncertainty estimates on phase velocity maps are needed to estimate the uncertainties of velocity profiles and, by extension, compositional inferences derived from such maps.

The solution ensemble provided by THBI allows us to quantify the uncertainty and trade-offs in the absolute phase velocity maps. The THBI approach to estimating phase dispersion maps is less biased by the artifacts of inversion (i.e., regularization and linearization) and incorporates both observational (measurement) and modeling uncertainty, constrained alongside the phase velocity uncertainties within the Bayesian inverse framework, differing from empirical approaches [e.g., *Bensen et al.*, 2009; *Shen et al.*, 2013; *Ekström*, 2014].

This statistical data set of phase dispersion maps can be used to propagate uncertainties into the next stage inversions for isotropic [e.g., *Yang et al.*, 2008, 2011; *Bensen et al.*, 2009; *Moschetti et al.*, 2010a; *Shen et al.*, 2013; *Shen and Ritzwoller*, 2016], and anisotropic [e.g., *Moschetti et al.*, 2010b; *Dalton and Gaherty*, 2013; *Lin and Schmandt*, 2014] compressional and shear wave velocities in the U.S. continental crust. Moreover, we can address questions that a typical geoscientist might ask: "To what degree will this data set inform existing crustal models?" or "In which regions of data availability will new crustal models derived from this data set differ from previous versions, within data uncertainty?"

We answer these questions by comparing the residuals derived from the THBI and those predicted by previous models. We assess regions within the U.S. where existing crustal models fit the new data set and regions where significant updates are required, based on the current level of uncertainty (i.e., probability distributions). We discuss how future geological and geophysical studies, which rely on existing crustal models, can assess the usefulness of these models, while highlighting which parts of the existing models will require significant updates.

2. Phase Velocity Measurements and Uncertainty

We use the data set of interstation phase velocity measurements reported by *Ekström* [2014]. These measurements are made from ambient noise Love and Rayleigh waves at 11 discrete periods between 5 and 40 s and are obtained by an automated frequency domain method using spatial autocorrelation (SPAC) [e.g., *Aki*, 1957; *Ekström et al.*, 2009; *Prieto et al.*, 2009; *Ekström*, 2014; *Menke and Jin*, 2015]. In its implementation, originally developed by *Aki* [1957] and extended by *Ekström et al.* [2009] and *Ekström* [2014], phase velocity dispersion curves for a pair of stations are extracted by fitting the zero crossings of the real part of the cross-correlation spectra to the zeros of a Bessel function of the first kind. The cross-correlation spectra are stacked from a large data set of 4 h long waveform records and are therefore resistant to strong earthquake signals. This study represents the most comprehensive data set of ambient noise phase velocity measurements across the continental United States to date. Compared to the time domain cross-correlation method [e.g., *Bensen et al.*, 2007], the SPAC method allows recovery of phase velocity measurements between closer station pairs [e.g., *Tsai and Moschetti*, 2010] (see also *Ekström* [2014] and Table 1).

Table 1. Parameters Used to set the Prior and Proposal Distributions of the rj-McMC of the THBI Including the Acceptance Ratios and Recovered Transdimensional, n, Parameters for the Three Independent Runs of the rj-McMC (Case 1, Case 2, and Case 3)[a]

| Love (L) Rayleigh (R) and Period | Acceptance Ratios in % ([b]B, D, M, C, N) | Mean of Posterior Distribution (n, σ) | | |
		Case 1	Case 2	Case 3[c]
1	L05	(22, 22, 50, 58, 33)	(234, 4.2)	(231, 4.2)	(386, 3.5)
2	L06	(19, 19, 43, 49, 28)	(204, 3.1)	(190, 3.4)	(373, 2.6)
3	L08	(18, 18, 43, 43, 27)	(170, 2.2)	(175, 2)	(313, 1.8)
4	L10	(17, 17, 42, 40, 27)	(132, 1.9)	(140, 1.7)	(217, 1.6)
5	L12	(17, 17, 46, 41, 30)	(116, 1.8)	(124, 1.7)	(200, 1.6)
6	L15	(15, 15, 40, 33, 27)	(116, 1.5)	(115, 1.5)	(193, 1.5)
7	L20	(14, 14, 41, 30, 28)	(96, 1.1)	(97, 1.1)	(120, 1.2)
8	L25	(11, 11, 36, 24, 25)	(85, 1)	(86, 1)	(104, 1.2)
9	L30	(10, 10, 34, 21, 22)	(92, 1.2)	(86, 1)	(93, 1.2)
10	L35	(9, 9, 36, 19, 21)	(71, 1.2)	(65, 1.1)	(66, 1.3)
11	L40	(7, 7, 38, 17, 20)	(54, 1.4)	(49, 1.3)	(49, 1.5)
12	R05	(21, 21, 49, 52, 31)	(183, 3.2)	(196, 3.1)	(316, 2.7)
13	R06	(19, 19, 47, 47, 30)	(146, 2.6)	(161, 2.5)	(304, 2.1)
14	R08	(17, 17, 42, 39, 27)	(134, 1.9)	(145, 1.7)	(251, 1.6)
15	R10	(17, 17, 43, 37, 27)	(108, 1.7)	(117, 1.5)	(194, 1.5)
16	R12	(17, 17, 45, 37, 30)	(107, 1.6)	(114, 1.6)	(183, 1.5)
17	R15	(14, 14, 37, 29, 27)	(105, 1.4)	(116, 1.3)	(183, 1.3)
18	R20	(13, 13, 38, 26, 28)	(111, 1)	(113, 1)	(159, 1)
19	R25	(11, 11, 33, 22, 25)	(115, 1.1)	(117, 1)	(154, 1.1)
20	R30	(10, 10, 33, 21, 25)	(113, 1.1)	(113, 1.1)	(144, 1.1)
21	R35	(9, 9, 34, 19, 24)	(95, 1.3)	(93, 1.1)	(108, 1.3)
22	R40	(9, 9, 36, 18, 23)	(81, 1.3)	(79, 1.3)	(86, 1.5)

[a]The similarity of the n value across the three independent cases is a heuristic justification for convergence. Bounds of uniform PDF used in the model priors. $(\sigma^L, \sigma^H) = (0.1, 10)$ and $(v^L, v^H) = (1.0, 6.0)$. Case 1 and Case 2: $(\sigma^L, \sigma^H) = (50{-}600)$, Case 3: $(\sigma^L, \sigma^H) = (50{-}200)$, proposal variances: $\Omega_\sigma = 0.5$, $\Omega_n = 1$, $\Omega_v = 1.0$. Case 1, Case 2, and Case 3: $N_S = 3 \times 10^6, 1 \times 10^7$, 1×10^7 and $N_R = 1000$, $N_C = 10$ (no. of parallel chains).
[b]B, Birth; D, Death; M, Move; C, Change; N, noise.
[c]In Case 3, the chain starts from the Ekström [2014] models sampled on an 1848 cell Voronoi tesellation.

In order to quantify reliably uncertainty in the phase dispersion maps, which will be used to statistically assess the predictive power of existing crustal models, we must estimate uncertainties associated with the underlying dispersion measurements. One approach is to assign measurement uncertainties empirically by assessing their repeatability or formal uncertainty using a single-mode assumption or isotropic distribution of noise sources [e.g., *Tsai and Moschetti*, 2010; *Ekström*, 2014]. However, the relevant data uncertainties result from a combination of measurement and modeling uncertainties, such as errors arising from the use of a ray theoretical approximation to model the spatial pattern of wave sensitivity. Therefore, we opt to estimate the aggregate data-related uncertainty explicitly, using a hierarchical Bayesian approach. We compare our Bayesian estimates of uncertainty to the empirical estimates of measurement uncertainty reported by *Ekström* [2014].

We conduct a series of numerical experiments, in which data uncertainty is allowed to vary with path length, to assess the relative contribution of measurement versus modeling uncertainty at each period. By estimating the level of uncertainty in the Bayesian inversion (a more conservative estimate, in most cases) we reduce the risk of mapping measurement errors into spurious features in the recovered phase velocity maps, especially for shorter periods where measurement uncertainties are large and strongly path length dependent (see section 4.3 for more details).

3. Transdimensional Inversion

The transdimensional hierarchical Bayesian inverse (THBI) method we employ is similar to that described by previous authors [e.g., *Bodin and Sambridge*, 2009; *Bodin et al.*, 2012b; *Young et al.*, 2013; *Saygin et al.*, 2016]. The THBI approach generates an ensemble of models that fit the data, unlike the classic least squares approach that produces a single optimal model using an a priori fixed parameterization. In the

Bayesian framework, a Monte Carlo sampler generates posterior distributions on model parameters from which an ensemble average and uncertainty and trade-off estimates are made. The term "transdimensional" implies that in addition to the typical model parameters (e.g., phase velocity values within a spatial domain), the model dimension (number of parameters required to represent phase velocity variations) is also constrained during the inversion [e.g., *Sambridge et al.*, 2006, 2012]. Voronoi tessellation is a discrete parameterization of the two-dimensional continuous seismic phase velocity field that captures velocity variations at irregular spatial scales [e.g., *Sambridge et al.*, 1995]. The tessellation partitions the plane into n nonoverlapping regions, using a nearest neighbor interpolation described by $3n$ parameters: a set of n velocity values $(v_i, . . , v_n)$ at nodal points described with $2n$ (longitude and latitude) location parameters (see Figure 1). It is this number n and the associated node coordinates that we wish to determine in the transdimensional step of the THBI method.

In the "hierarchical-Bayes" step, at each period, we include an extra parameter (σ: the uncertainty (noise) scaling—equation (2)) to be constrained by the data during the Bayesian inversion. This parameter is considered a "hierarchical" parameter because it sits at a higher level in the inversion process. It is estimated before calculating the model fit of predicted to observed data for each velocity update step (i.e., lower level model parameters) that contributes to the final two-dimensional phase velocity map [e.g., *Malinverno and Briggs*, 2004; *Malinverno and Parker*, 2006; *Bodin et al.*, 2012b]. Contributions of measurement and modeling uncertainties are quantified by rerunning the chain for three different subsets of the data, assigning different σ values for the different subsets: short, medium, and long path lengths (see Table 2 for cutoff limits in km). This analysis shows that the hierarchical parameter is dominated by measurement uncertainty, which is strongly path dependent (see section 4.3 for details).

On the whole, the Bayesian approach describes a posterior probability density function, $p(\boldsymbol{m}|d)$, on three classes of model parameters, $\boldsymbol{m} = \{\sigma, \boldsymbol{n}, \text{ and } \boldsymbol{v_i}\}$ (i.e., noise σ, model dimension n, and phase velocity values at the nodal points, v_i) given as follows:

$$p(\boldsymbol{m}|d) \propto p(d|\boldsymbol{m})p(\boldsymbol{m}), \tag{1}$$

where $p(d|\boldsymbol{m})$ is the likelihood function, which describes the probability of the predicted model given the observed data, d (and includes the hierarchical noise parameter σ):

$$p(d|\boldsymbol{m}) \propto \exp - \left\{ \frac{\|g(\boldsymbol{m}) - d\|^2}{2\sigma^2} \right\} \tag{2}$$

In our forward calculation of the predicted travel times, $g(\boldsymbol{m})$, we approximate the geographical sensitivity of waves between station pairs by great circles, rather than using finite frequency kernels. A uniform probability density function, $p(\boldsymbol{m})$, describes our prior information on the model parameters, and in the case of the phase velocity is represented by a range that encompasses all possible values for each period range (see Table 1), while for the noise and model dimension parameters, we use a range wide enough to include the most likely value, after an initial trial and error process. We sample the posterior probability distribution using a variation of the Metropolis Hastings method known as the reversible jump Markov chain Monte Carlo (rj-McMC) algorithm that explores a probability space with varying dimensions [e.g., *Green*, 1995, 2003]. There are five kinds of proposal steps in the rj-McMC, with each proposal step selected with equal probability (see overview in Figure 1): the first three steps involve the proposal of a new model $\boldsymbol{m_p}$ by a "transdimensional" transformation step where the number, n, or configuration of the cells are changed (via (1) birth, (2) death, or (3) move); and the last two steps involve (4) a fixed-dimension transformation step (changing a cell velocity value, $\boldsymbol{v_i}$) or (5) a hierarchical step (changing the noise scaling parameter, λ_j in $\sigma = \lambda_j\sigma$).

Each new model in the proposal step, $\boldsymbol{m_p}$, is sampled from a Gaussian distribution, $q(\boldsymbol{m_p}|\boldsymbol{m_j})$, which requires the perturbation of the preceding model, $\boldsymbol{m_j}$, using proposal variances, $\boldsymbol{\Omega_m}$(one for each model type: $\boldsymbol{\Omega_\sigma}$, $\boldsymbol{\Omega_n}$, $\boldsymbol{\Omega_v}$):

$$\boldsymbol{m_p} = \boldsymbol{m_j} + u\boldsymbol{\Omega_m}, \tag{3}$$

where u is drawn from a Gaussian distribution $N(0,1)$. With the prior distribution and the proposal variations set, the evolution of the chain is then governed by the acceptance probability, $\boldsymbol{A}(\boldsymbol{m_p}|\boldsymbol{m_j})$, which determines whether or not the current model, $\boldsymbol{m_j}$, will be retained or replaced by the proposed model $\boldsymbol{m_p}$. This happens if $\boldsymbol{U} \leq \boldsymbol{A}(\boldsymbol{m_p}|\boldsymbol{m_j})$, where $\boldsymbol{U}$ is a random number generated from a uniform distribution between 0 and 1 (for a
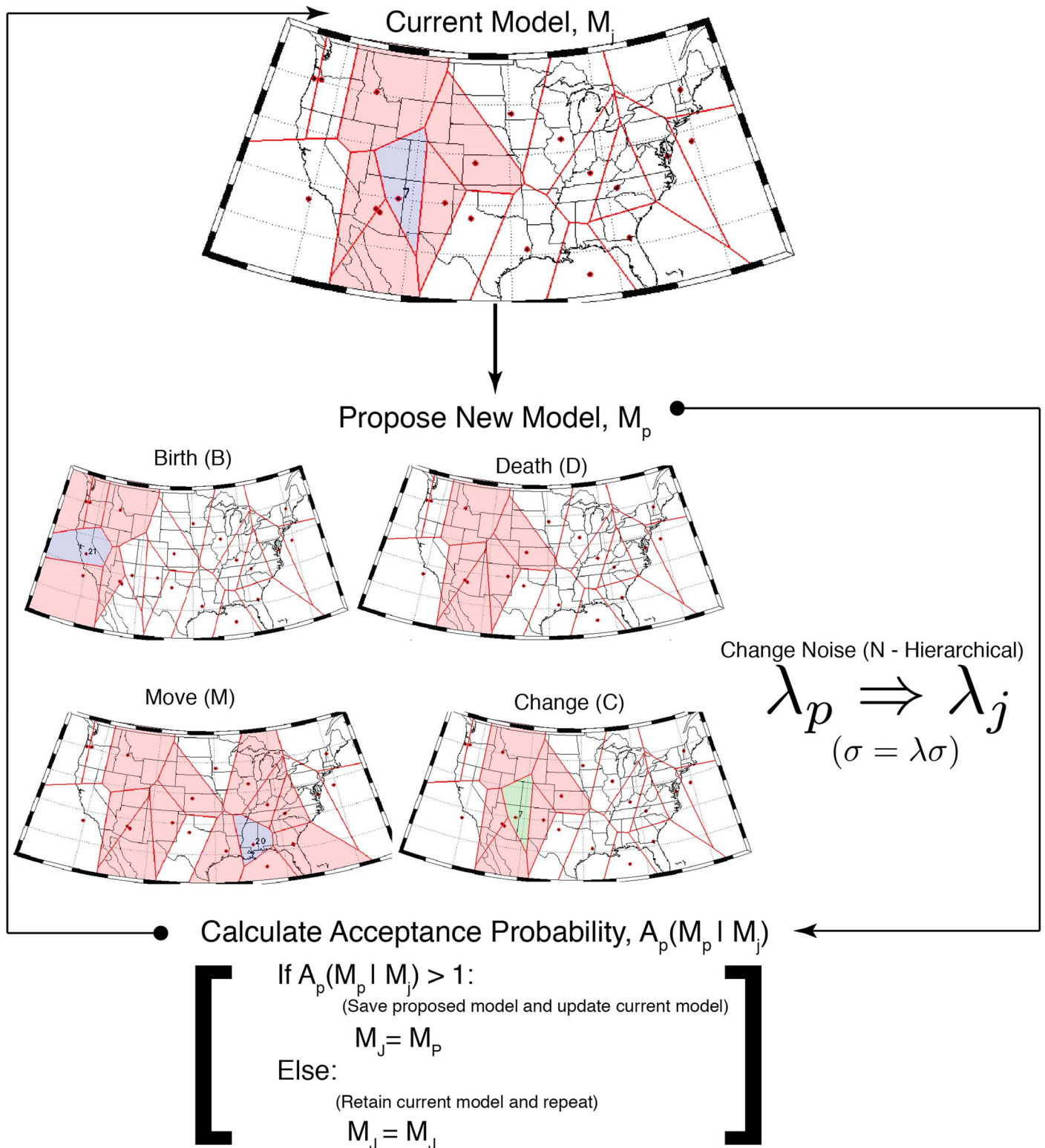
Figure 1. This flowchart illustrates how transdimensional hierarchical Bayesian inversion works. (top) The current model M_j is initialized from a random state or saved from a previous proposal step, showing the Voronoi tessellation with $n = 20$ nodal points (dots) and constant value cells (outlined polygons). The Voronoi cell colored blue is transformed during the proposal steps. (middle row) A new model M_p is proposed using one of five different types of transformation steps: Birth (B), Death (D), Move (M), Change(C), or Change Noise (N). The first three transformations are "transdimensional" steps because they involve a change in the dimension (number of Voronoi cells, n, required to describe the velocity domain). The proposal step can also involve a change in the cell velocity (C) and the noise scaling parameter $\sigma_j = \lambda_j \sigma$. The adjacent cells (colored red) are the only ones affected by the proposal step.

Table 2. Sources of Uncertainties: Comparing the Hierarchical Noise Parameter for Three Different Subset of Data: Short, Medium, and Long Path Lengths (SP, MP, and LP) for 5 s, 10 s, and 40 s Love and Raleigh Waves[a]

	Love (L) Rayleigh (R) and Period	Distance Range (km) (SP, MP, LP)	No. of Observation (SP, MP, LP)	Hierarchical σ Value THBI (s) (SP, MP, LP)	Empirical Value From Ekström (s) (SP, MP, LP)
1	L05	(20–100, 100–150, 150–300)	(2956, 3847, 4792)	$4.23^{\pm0.42}$ $3.98^{\pm0.43}$ $3.46^{\pm0.40}$	$0.33^{\pm0.34}$ $0.54^{\pm0.48}$ $0.66^{\pm0.50}$
2	L10	(20–130, 130–165, 165–300)	(3348, 4952, 3616)	$1.87^{\pm0.34}$ $1.57^{\pm0.31}$ $1.50^{\pm0.31}$	$0.39^{\pm0.65}$ $0.50^{\pm0.66}$ $0.60^{\pm0.70}$
3	L40	(100–429, 429–520, 520–700)	(7975, 8448, 7879)	$1.57^{\pm0.31}$ $1.43^{\pm0.30}$ $1.32^{\pm0.30}$	$0.97^{\pm0.40}$ $1.17^{\pm0.33}$ $1.36^{\pm0.29}$
4	R05	(20–100, 100–150, 150–300)	(2562, 3823, 4775)	$2.93^{\pm0.37}$ $2.99^{\pm0.39}$ $2.52^{\pm0.37}$	$0.33^{\pm0.33}$ $0.54^{\pm0.50}$ $0.68^{\pm0.58}$
5	R10	(20–130, 130–165, 165–300)	(3461, 4897, 3667)	$1.73^{\pm0.33}$ $1.45^{\pm0.30}$ $1.37^{\pm0.30}$	$0.38^{\pm0.48}$ $0.55^{\pm0.83}$ $0.66^{\pm0.80}$
6	R40	(100–429, 429–520, 520–700)	(17030, 23202, 24143)	$1.55^{\pm0.29}$ $1.32^{\pm0.28}$ $1.24^{\pm0.28}$	$1.04^{\pm0.35}$ $1.29^{\pm0.37}$ $1.48^{\pm0.33}$

[a]Distance range is the interstation distance used in the particular subset of data. Number of observations measures the count of observations belonging in each data set. The recovered hierarchical noise (and standard deviation) from THBI is compared with empirical value (derived from propagating phase velocity uncertainty in *Ekström* [2014]) (see also Figure 6b). SP = Short path, MP = Medium path, and LP = Long path.

complete discussion of how the acceptance probability, proposal distributions, and prior distributions are defined see *Bodin et al.* [2012a, 2012b]). The range of the prior distribution and the proposal variances are the only free parameters to be selected, and they are chosen to balance the convergence rate with efficient sampling of the model space (Table 1).

3.1. THBI Applied to the USArray Data Set

Figure 2 shows snapshots along the Markov chain as it samples the posterior distribution of the 5 s phase velocity map for Love waves. Because achieving convergence is key for obtaining reliable model mean and
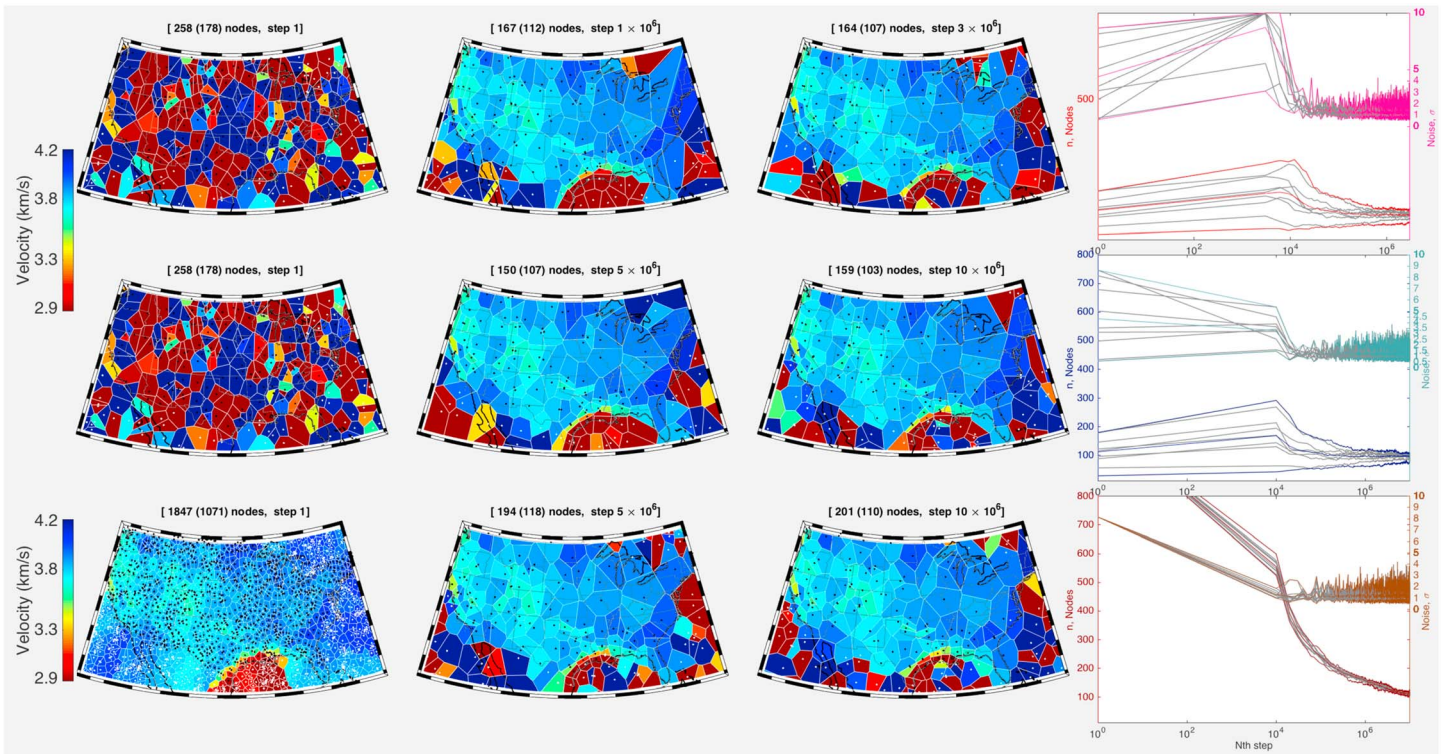
Figure 2. Transdimensional inversion applied to the USArray data set of 5 s Rayleigh wave phase velocity measurements (scale bar is in km/s). (Columns 1 to 3) Snapshots showing the evolution of the model parameterization (Voronoi cell distribution) along 1 of the 10 parallel Markov chains. The nodes inside the data space are marked black, while those outside are white. The labels on top of each plot show the total nodes (with internal nodes in parentheses). Each of the chains is initialized using two different starting models: (Rows 1 and 2) initial cell distribution sampled from an a priori random normal distribution, and (Row 3) starting model of 1847 randomly spaced nodes sampled on the *Ekström* [2014] phase velocity map. (Column 4) Time series history of the number of internal Voronoi nodes (dimension), n (left axis), and hierarchical parameter, σ (right axis) along 10 parallel Markov chain (gray lines). The minimum, maximum, and mean values are displayed as the colored lines. The chain converges when the number of nodes reaches a mean value, and we mark this point forward as the post burn-in steps (the high-resolution mean phase velocity and standard deviation maps are obtained from averaging all accepted models, across all chains, after burn-in: see Table 1).

uncertainty estimates, we use three different modeling approaches: running either (1) 10 parallel chains run for 3 million steps initialized from a random start state drawn from a uniform prior distribution with 379 Voronoi nodes, (2) the same procedures as Case 1 but using 10 million steps in each chain, and (3) 10 parallel chains run for 10 million steps but initialized from a high-density (1847 node) discretization of the mean map reported by *Ekström* [2014]. In all cases, the chain takes only ~100,000 steps to converge to an optimal state (through birth, death, move, and cell change steps). Somewhat surprisingly, the nodal density, misfit, and other key inversion parameters are similar across solutions, independent of the starting state (see Figure 2 and Table 1), suggesting that global convergence is achieved and that the posterior ensemble is representative $p(\boldsymbol{m}|d)$. The same solution is recovered for modeling approach 3, despite using a high-density starting model, demonstrating that the THBI always produces a parsimonious solution; i.e., it looks for model to fit the data using the simplest parameterization possible. The time to reach this optimal state is called the burn-in period, and only models that are generated after this period (post burn-in) are used to build the posterior distribution and derive the final ensemble average of mean, standard deviation, and trade-off maps. During the sampling, only model updates that change the data misfit are accepted as valid proposal steps. This ensures that regions with no data are locked in (i.e., white dots in Figure 2).

3.2. Mean and Standard Deviation Phase Velocity Maps

In our construction of the mean and standard deviation maps, we sparsely resample the ensemble to ensure that the aggregated models are not correlated. First, we construct high-resolution mean phase velocity maps by interpolating the Voronoi tessellation on a regular 600×600 grid, using only the post burn-in samples from the multiple chains. The total number of samples used in the averaging scheme, N_T, is a function of the total number of steps per chain, N_S, the number of independent Markov chains, N_C, the number of burn-in steps, N_B, and the resampling rate N_R:

$$N_T = \left(\frac{N_S - N_B}{N_R} \right) \times N_C$$

The final ensemble is resampled at every thousandth step ($N_R = 1000$) to ensure that models used in the final average are not correlated. For example, in the longest run of the 5 s Love wave, the total number of samples used to produce the mean phase velocity map is $N_T \sim 10^4$ ($N_s = 10^7$, $N_R = 10^3$, $N_B = 10^6$, and $N_C = 10^1$) (Figure 3). In the run for Case 3, the convergence is faster (smaller burn-in steps compared to Case 1 and Case 2), since the starting model is already close to the true solution. We report the number of burn-in steps, the postconvergence nodal density, and the postconvergence hierarchical noise parameter for the other Love and Rayleigh maps in Table 1.

Next, we use the mean phase velocity maps to derive the standard deviation maps (using similar post burn-in ensemble and resampling strategy). Areas in these maps with low standard deviation show which parts of the average models in Figure 3 are well constrained. Large uncertainties in regions with no data are trivial to explain; however, where data exist, there are some regions of high standard deviation. The outline of these high standard deviation regions is similar to features in the mean models associated with velocity gradients. We therefore compute a spatial gradient of the velocity fields for comparison with the standard deviation maps. A high correlation between these two maps confirms our intuition that high gradients contribute to high uncertainty (Column 2 versus Column 1 in Figure 4).

3.3. Monte Carlo Search Efficiency

As described above, during the rj-McMC sampling, each of the five steps in the THBI has an equal likelihood of being selected (see Figure 1), and for each model proposed, the ratio of acceptance is determined by the prescribed proposal variances, $\boldsymbol{\Omega_m}$, (e.g., equation (3) in section 3). The search efficiency can be quantified by the acceptance ratios (ratio of number of proposed models to accepted models, see Table 1).

We observe that for both the Love and Rayleigh wave inversions, the move or change steps have the highest acceptance ratios (as large as 50%), followed by the hierarchical step (~30%) and the birth/death step (~20%). Compared to the change step, the move step is preferred, especially for periods >10 s. This is because it is easier to improve the data fit using a move step compared to a change step. At longer periods, the acceptance ratio decreases, suggesting that for the chosen proposal variances, it takes longer to find good models
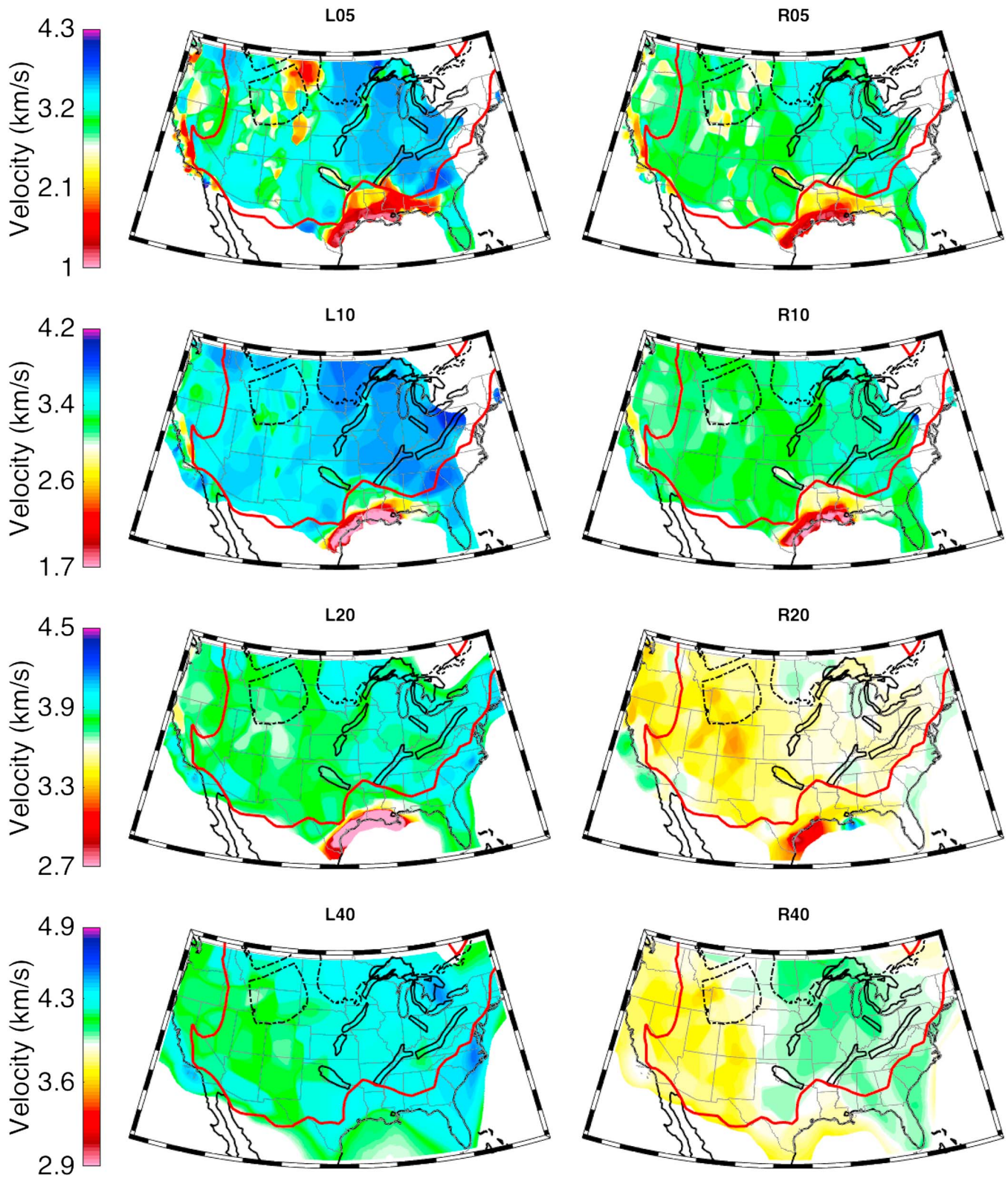
Figure 3. Mean phase velocity maps for (left) Love and (right) Rayleigh waves at 5, 10, 20, and 40 s. The mean maps are reported in absolute phase velocity measurements, given the inversion does not start from a reference mean velocity value; the velocity range is chosen to accentuate maximum velocity variation. The outlines of the major tectonic divisions are from *Whitmeyer and Karlstrom* [2007]: Precambrian basement (red), midcontinental rift, Oklahoma aulacogen, and the Reelfoot Rift (solid outline) and Archean cratons >2.5 Ga (dashed).
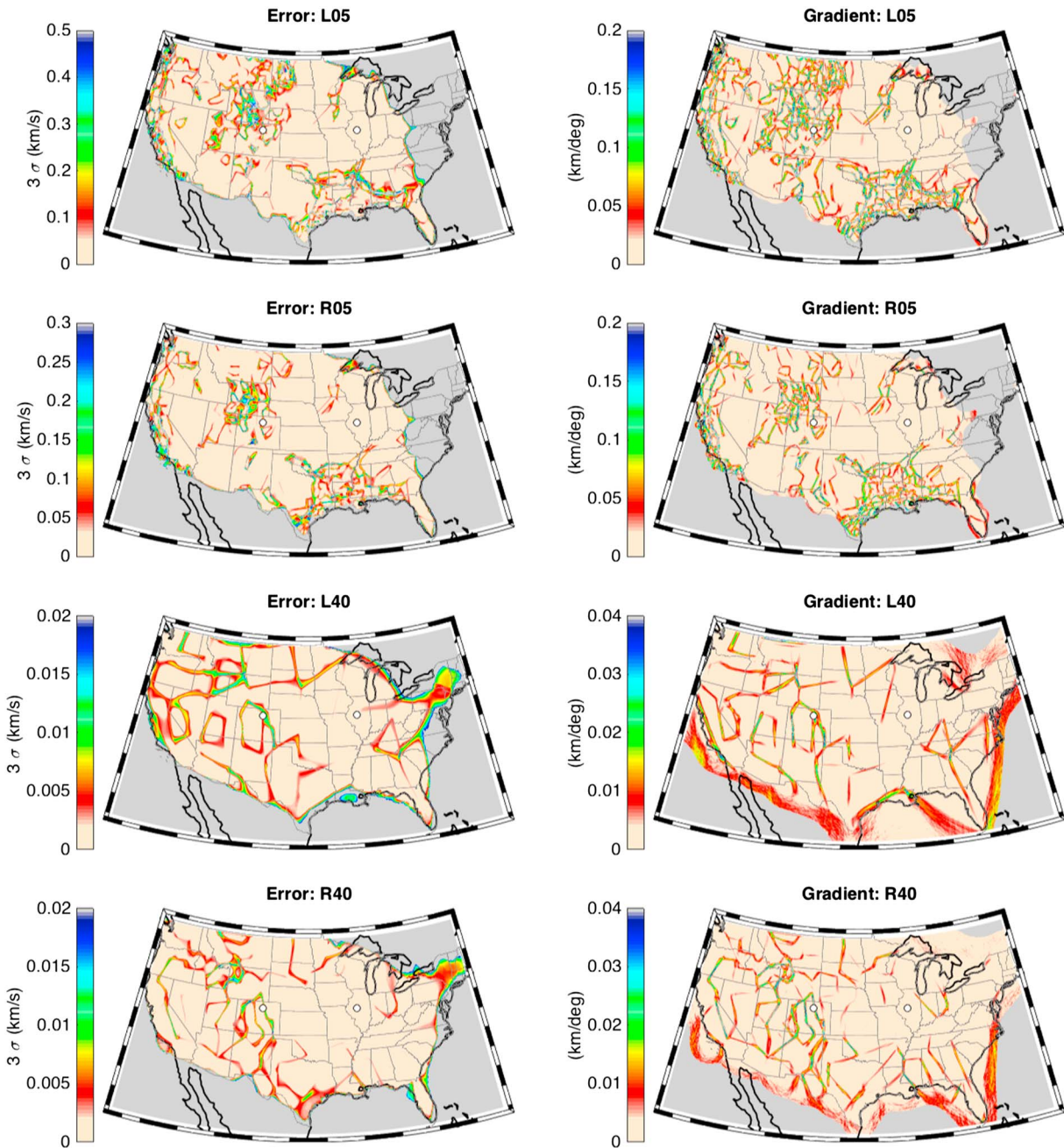
Figure 4. Standard deviation maps (at 3σ level) and the associated 2-D spatial gradient of the mean phase velocity maps obtained in Figure 3 (color scale bar is in km/s). (Rows 1 and 2) Short-period (5 s) Love and Rayleigh phase velocity maps have the largest standard deviations. (Rows 3 and 4). The longest periods (40 s) maps with reduced amplitude for both standard deviation and spatial gradient. The correlation between high standard deviations and spatial gradient is visible. The two locations on the map represented by the circle are for Colorado (left) and Illinois (right). The full probability density functions at these locations are described in Figure 6.

as the period increases. This is not the case for the move step. Similar to the change step, the acceptance ratio of the birth/death step decreases with period for the same reason. The acceptance ratio for the hierarchical step is only weakly dependent on the period, suggesting that the proposal variance used in this step is suitable across all periods for both Love and Rayleigh wave using the THBI approach (Table 1).

Taken together, the acceptance ratios show that at longer periods, it takes longer for the inversion to converge (see Figure 2). This can be understood by the fact that at longer periods, the interstation raypaths are longer and so will cross over multiple Voronoi cells. Therefore, finding the right combination of velocity values within all cells for all crossing paths becomes more challenging (the acceptance ratio for Case 3 is

larger since the chain starts from an optimal model; see supporting information Table S1). Following the recommendation of *Ray et al.* [2013], we increase the acceptance ratio of the birth/death step by decreasing the proposal step size, $\mathbf{\Omega_v}$, from 1.0 to 0.1; we also reduce the prior range, (v^L and v^H), (from 1.0–6.0 km/s to 2.0–4.5 km/s). These new parameters improve the acceptance ratio for the longer period maps.

3.4. Spatiospectral Comparison of Phase Velocity Maps

To quantify the differences in the results of the two inversion methods (i.e., THBI versus least squares), we conduct spatiospectral analysis of the phase velocity maps using the multiple spherical, Slepian taper approach described in, e.g., *Simons et al.* [2006] and *Dahlen and Simons* [2007]. Spatiospectral analysis is analogous to power spectral analysis with spherical harmonics, except that the power spectrum is estimated over a region, R, on the Earth surface (continental USA) instead of over the entire globe. The use of multiple spherical, Slepian tapers in the spatial domain avoids the deleterious effects of ringing that arise from truncating the velocity field abruptly during windowing [e.g., *Meschede and Romanowicz*, 2015]. We define a spatial band limit of $L = 18$, compute the associated tapers, $g_\alpha(\boldsymbol{r})$, which are optimally concentrated within the region of data availability, and multiply the phase velocity field $v(\boldsymbol{r})$ by $g_\alpha(\boldsymbol{r})$ before computing the multitaper spectral estimate, $\hat{S}_l^{MT}$, which is averaged over the single tapered spectral estimates, $\hat{S}_l^\alpha$ up to harmonic degree $l = 200$ using the expressions from equations 130 and 139 of *Dahlen and Simons* [2007] (see Figure 5):

$$\hat{S}_l^\alpha = \frac{1}{2l+1} \sum_m \left| \int_\Omega g_\alpha(\boldsymbol{r}) v(\boldsymbol{r}) Y_{lm}^*(\boldsymbol{r}) \mathrm{d}\Omega \right|^2 \tag{4}$$

$$\hat{S}_l^{MT} = \sum_\alpha c_\alpha \hat{S}_l^\alpha \quad \text{where} \quad \sum_\alpha c_\alpha = 1 \tag{5}$$

We compare the multitaper spectral estimate across the two different inversion approaches using the across-model correlation measure [e.g., *Becker and Boschi*, 2002]. Differences in the wavelength, power, and resolution aliasing that are introduced by making a priori assumptions in regularization like damping or smoothing for the least squares approach or in the conservative estimate of uncertainty derived during the hierarchical step of the THBI approach are explored and discussed in detail (see section 4.3).

4. Results

In addition to typically reported optimal (mean) phase velocity maps, we report the standard deviation phase velocity maps for Love and Rayleigh waves as well as the posterior distribution functions for the other class of model parameters (σ and $\boldsymbol{n}$). These model parameters show interesting patterns that are dependent on wavelength (or period) of the surface waves and the length scale of velocity variation. Spectral analysis of the phase velocity maps derived from THBI and least squares methods shows an overall consistency, especially for Rayleigh waves while revealing other sources of differences, which we explore in detail. We show the results of the statistical assessment of the crustal models with an emphasis on utility for geological inference and updates in regionalization and shallow structure.

4.1. Model Uncertainties: Data Coverage and Spatial Gradients

We recover the largest velocity variations and smallest length-scale features at the shortest period for the Love waves (5 s) similar to the results reported by *Ekström* [2014]. We obtain additional information on the sources of the uncertainty in the phase velocity maps by comparing the standard deviation maps to the maps of the spatial gradient. The largest standard deviations (>0.5 km/s) describe portions of the map that are not constrained by data (Figure 4). In regions having good data coverage, the largest standard deviations occur at largest velocity gradients, for instance at boundaries of slow to high phase velocities, e.g., along the low velocities in the Mississippi embayment, North Dakota, and in the Rockies and Sierra Nevada mountains. This feature is unique to tomography where the ray propagation or model parameterization is not fixed during the inversion, and it is attributable to trade-offs between the location of the velocity gradients and its amplitudes when the only constraint is interstation travel time measurements [e.g., *Galetti et al.*, 2015]. The actual probability distributions across these boundaries are more complex as described below.

### 4.2. Non-Gaussian Errors in Phase Dispersion Curves

A better understanding of the uncertainties in the phase velocity measurements can be gained by evaluating the posterior probability density function (PDF) of the model parameters. The posterior PDFs of the phase
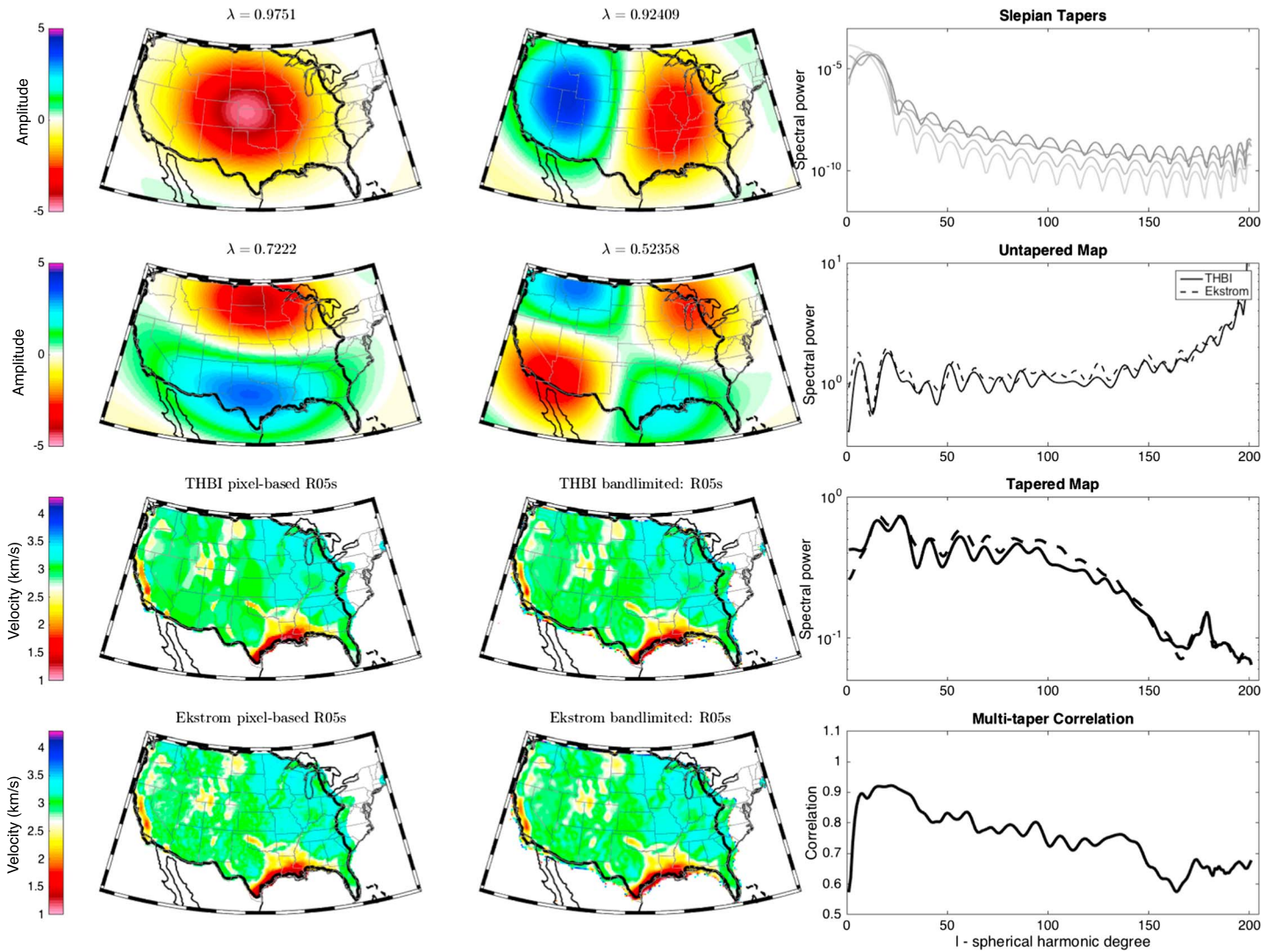
Figure 5. Spatiospectral analysis using multiple Slepian windowing tapers on the region R (thick black outline), defined by data availability in the conterminous U.S. (Rows 1 and 2) First four optimally concentrated Slepian tapers (λ is the concentration factor). (Rows 3 and 4) Phase velocity maps of 5 s Raleigh waves for the THBI (Row 3) and *Ekström* approach (Row 4) showing the pixel-based maps (Column 1) and filtered at a spherical harmonic cutoff of $l = 200$ (the Slepian tapers are applied before estimation of spectral power, see Column 3). (Column 3, first panel) Spectrum of first four Slepian tapers with increasing spectral leakage (increasing shades of gray) applied to the phase velocity maps (taper bandwidth $L = 18$). (Column 3, second panel) Spectrum of untapered maps: solid line for THBI and dashed line for Ekström. (Column 3, third panel) The spectrum of the tapered maps (gray lines matching first panel) showing the Eigen value-scaled multitaper average as thicker lines. (Column 3, fourth panel) Multitaper correlation between the two tapered maps.

velocities are compared at two locations in the U.S.: Colorado and Illinois. The coordinates in Colorado are chosen to coincide with a region of high posterior standard deviation, while those in Illinois are chosen to be representative of a region with small posterior standard deviation (see phase velocity maps for 5 s Love and Rayleigh wave in Figure 3). In Colorado, we observe a strongly multimodal distribution especially for the Love waves. The mean velocity of 2.82 km/s, computed during ensemble averaging, is intermediate between two equally likely modes: 2.5 km/s and 3.1 km/s (Figure 6). The uncertainties decrease as the wavelength increases, with the Love wave having larger uncertainties than Rayleigh waves.

The typical assumption of Gaussian errors used in linear least squares inversion [e.g., *Menke*, 2012] clearly does not hold for the 5 s Love wave phase velocity at the Colorado location. By contrast, the 5 s Rayleigh wave can be fairly described by a Gaussian distribution centered on a mean phase velocity value of 2.76 km/s (Figure 6). At other periods, the PDF can vary from a single mode to bimodal, for both Love and Rayleigh waves. The ability of the THBI approach to recover spatially dependent probabilities is a particularly useful advantage.
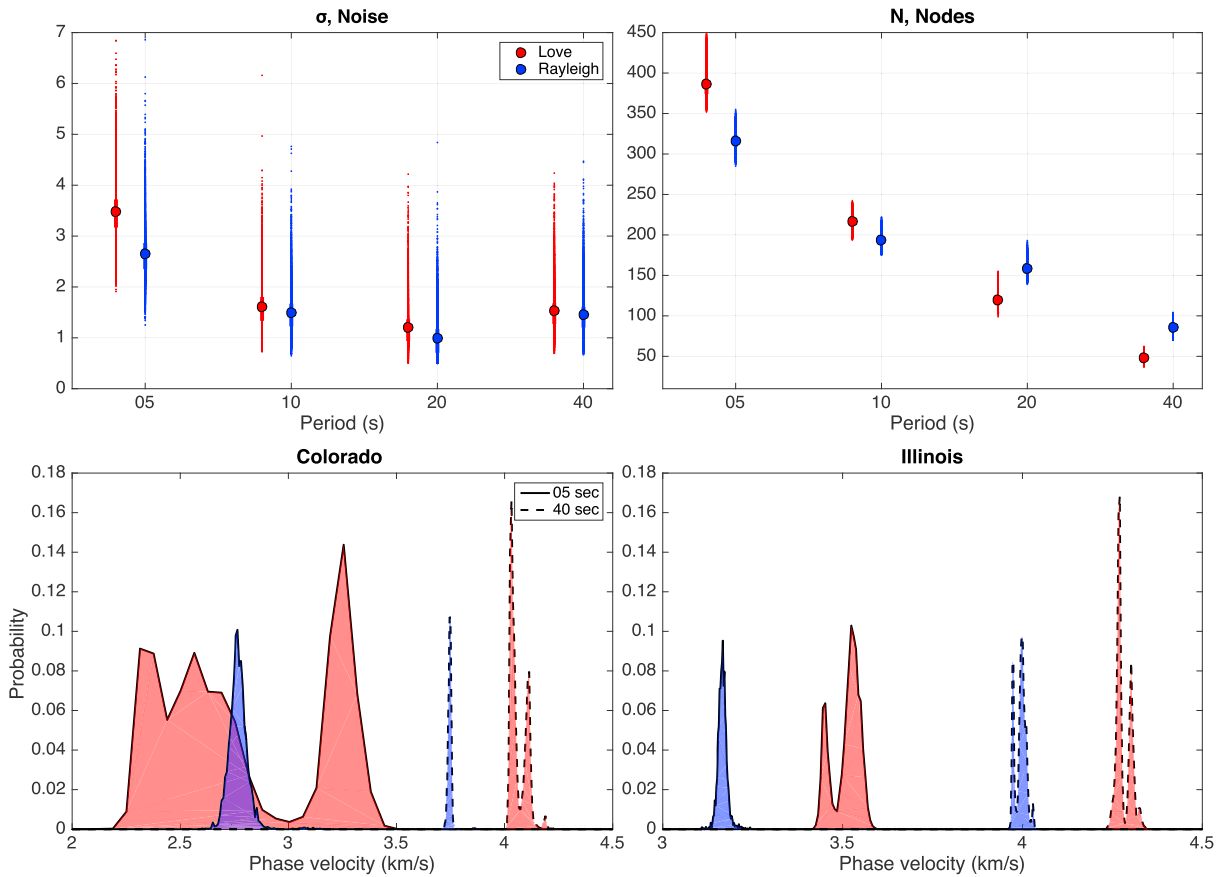
Figure 6. Probability density functions (PDF) of the hierarchical parameter, count of Voronoi nodes, and phase velocity (at Illinois and Colorado: cf. Figures 3 and 4) for both Love (red) and Rayleigh (blue) waves. (Row 1, Column 1) PDF of the hierarchical noise parameter expressed as a boxplot. (Row 1, Column 2) PDF of the count of the Voronoi nodes expressed as a boxplot. The height of the boxplot encompasses 99% of the values, while the outliers are represented by small dots. The mean is shown as the large circles over the boxplot. (Row 2) PDF of phase velocity values at Illinois (Column 1) and Colorado (Column 2) for 5 s and 40 s Love and Rayleigh waves.

4.3. Sources of Uncertainties in the Hierarchical (Noise) Parameter: Contributions From Measurement and Modeling Errors

Errors associated with the measurement of phase velocity dispersion and ray-theoretical forward modeling during inversion of the maps can affect the details of the recovered model. In the THBI approach, these errors are jointly quantified in the hierarchical noise parameter, σ, and estimated during the hierarchical step of the Markov chain (see Figure 1). We observe that the σ value for Love waves is systematically greater than for Rayleigh waves and decreases with increasing period (Figure 7). A higher σ value for Love compared to Rayleigh waves is due, in part, to the larger relative observational errors of the spatial autocorrelation measurements at shorter paths [e.g., *Ekström*, 2014], and possibly also the potential contamination of overtones on Love waves compared to Rayleigh waves [e.g., *Foster et al.*, 2014]. It could also be due to the modeling errors. For example, we assume that the raypaths are straight, but since the variation is largest for Love waves, especially at shorter periods, this assumption may be invalid, leading to higher modeling uncertainties captured by the noise parameter.

To distinguish between the measurement and modeling uncertainties, we rerun the THBI analysis on three different subsets of the data (sorted based on interstation distance: short, medium, and long path lengths (see Table 2 for details). If modeling uncertainty dominated over the measurement uncertainty, we would expect the recovered hierarchical parameter to be greater at longer path lengths, since the modeling error is expected to increase with path length [e.g., *Bodin et al.*, 2012b, Figure 8]. We observe the opposite trend: the largest uncertainties are observed at the shortest path lengths and at the smallest wavelength, in
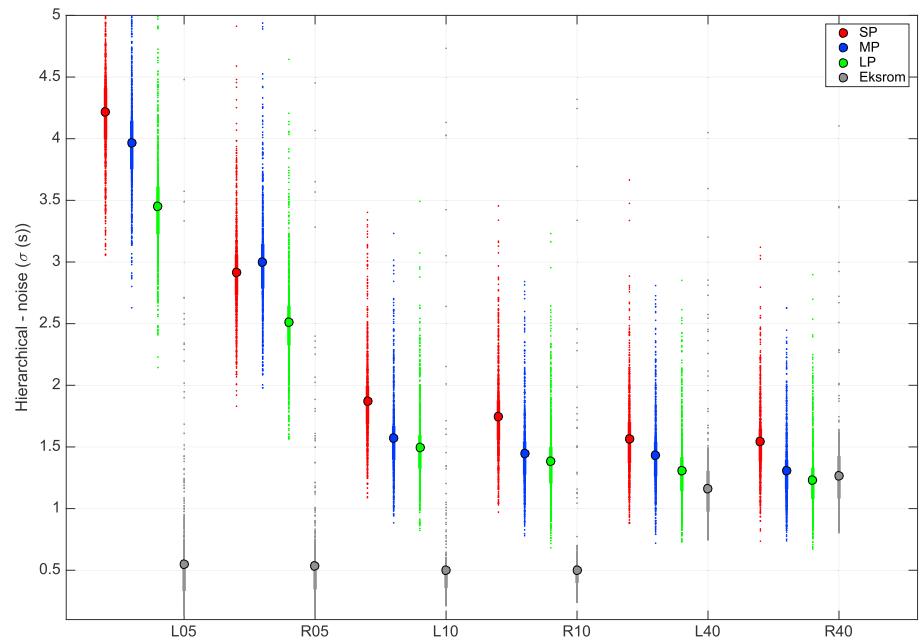
Figure 7. Data uncertainty based on probability distribution function of the hierarchical (noise) parameter for three different groups of interstation distance: short (SP: red), medium (MP: blue), and long (LP: green) path lengths. The filled circles represent the mean values for each group. The empirical estimate of travel time uncertainty propagated from phase velocity uncertainty reported by *Ekström* [2014] is shown in gray (see Table 2 for details). Only at the longest wavelength and longest path data do the two estimates agree.

particular, short interstation distance 5 s Love waves (Figure 7). As interstation distance decreases, the estimated uncertainty increases. This pattern persists at all periods for both Love and Rayleigh waves, with decreasing uncertainties as wavelength increases. This suggests that the dominant source of uncertainty is measurement uncertainty. Furthermore, our results support the notion that making phase velocity measurements at shorter periods and for shorter interstation distances is more difficult than at longer periods, and the inferred uncertainty is able to account for this uncertainty in the inversion. The recovered uncertainties from THBI are larger than the empirical estimates reported in *Ekström* [2014] (Figure 6). This difference may reflect the fact that the THBI uses only a single σ value to represent a distribution that contains outliers (gray boxplot in Figure 7). Nevertheless, we believe that the THBI uncertainty estimate should be less subjective, since it is constrained during inversion by the data itself, rather than subjectively assessed by an operator. The inverse dependence on path length suggests that the larger influence of measurement uncertainty over modeling uncertainty is an inference that is not straightforwardly accessible using empirical arguments only.

4.4. Autoadaptive Parameterization Independent of Data Coverage

In the Bayesian inversion used in this study, the model parameterization is autoadaptive (i.e., recovered by the data) and reflects the true amplitude of phase velocity variations in the Earth model. We see that the number of Voronoi cells (nodes) required to parameterize the phase velocity model efficiently decreases with increasing period and is governed by the spatial scale of velocity variation in the model space (node panel in Figure 6). The autoadaptive nature is compelling when we see that the number of nodes needed to represent Love waves is larger than that for Rayleigh waves, since the amplitude of velocity variations are greater for Love waves than for Rayleigh waves (cf. red versus blue in node panel of Figure 6). A special transition happens at periods greater than 20 s where the numbers of nodes for Rayleigh waves become larger than those for Love waves. A comparison of the phase maps of Rayleigh to that of Love at this period explains this pattern, since the pattern switches and amplitude of velocity variation for Rayleigh becomes larger than Love at this period (cf. node panel in Figure 6 with maps in Figure 3). Simply put, model parameterizations (tessellations) based on prior considerations like data coverage density do not appear to be appropriate for constructing phase velocity maps (data coverage is uniform, yet nodal density adapts to model complexity).
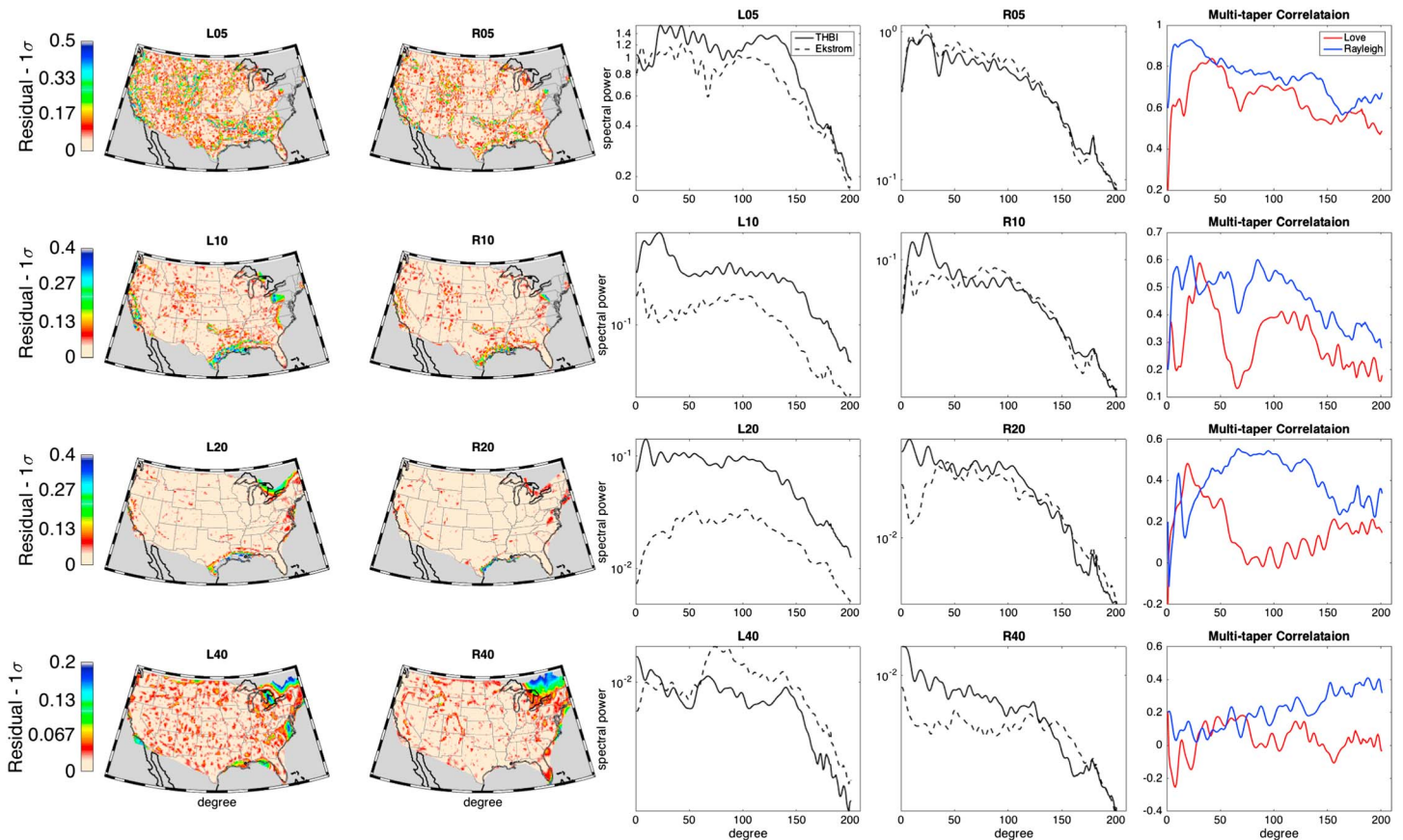
Figure 8. A comparison between the THBI and least squares results of *Ekström* [2014] using residual maps and spectral analysis. (Columns 1 and 2) Difference of THBI standard deviation and Ekstrom minus THBI residual maps resampled at the same resolution as the least squares maps (0.25° × 0.25°). (Columns 3 and 4) The spectrum of the tapered Rayleigh (Column 4) and Love wave phase velocity maps (Column 3) for the THBI (solid line) and *Ekström* (dashed line) model. (Column 5) The multitaper correlation across the different spherical harmonic degrees for both Rayleigh and Love wave up to degree $l = 200$.

4.5. Comparison to Least Squares Inversion

The THBI approach does not require any explicit regularization (smoothing or damping); neither does it require the measurement uncertainties to be set a priori. Despite this lack of preconditioning, our phase velocity maps are qualitatively and visually similar to those obtained by the least squares approach [e.g., *Ekström*, 2014]. Some minor differences exist, however, and we investigate these differences (and the sources) by conducting two analyses: (1) calculating pixel-based residual maps and (2) evaluating multitaper spectral and correlation analysis. A comparison of the residual maps to the standard deviation maps shows that the differences are statistically insignificant (Columns 1 and 2 of Figure 8). We observe negligible speckling in the residual maps, with the amplitude reducing as period increases (Figure 8). This feature may reflect an artifact of the least squares inversion, which is conducted on a high-resolution 0.25 by 0.25° grid. For short-period phase velocity maps there are different wavelengths of velocity variation (e.g., see variable nodal density in Figure 2), and applying a single damping and smoothing coefficient results in small-scale variation in the residual maps. Reduction in speckling at longer periods is consistent with the fact that the wavelength of velocity variation is more uniform.

The spectral analysis and multitaper spectral correlation allows us to quantify the differences (and similarities) across various wavelengths, which are introduced by inverting the phase velocity maps using the different approaches. The spectral amplitude for the Rayleigh wave maps is well correlated across all periods (Columns 3 and 4 of Figure 8), with total correlation reducing at longer periods. Compared to the Rayleigh wave phase velocity maps, the Love wave maps are less correlated at intermediate periods (20 s and 40 s; Columns 3 and 4 of Figure 8). The reduction in correlation is partly due to the difference in the very short wavelength low velocity structure within the Mississippi embayment (see Figure 9).
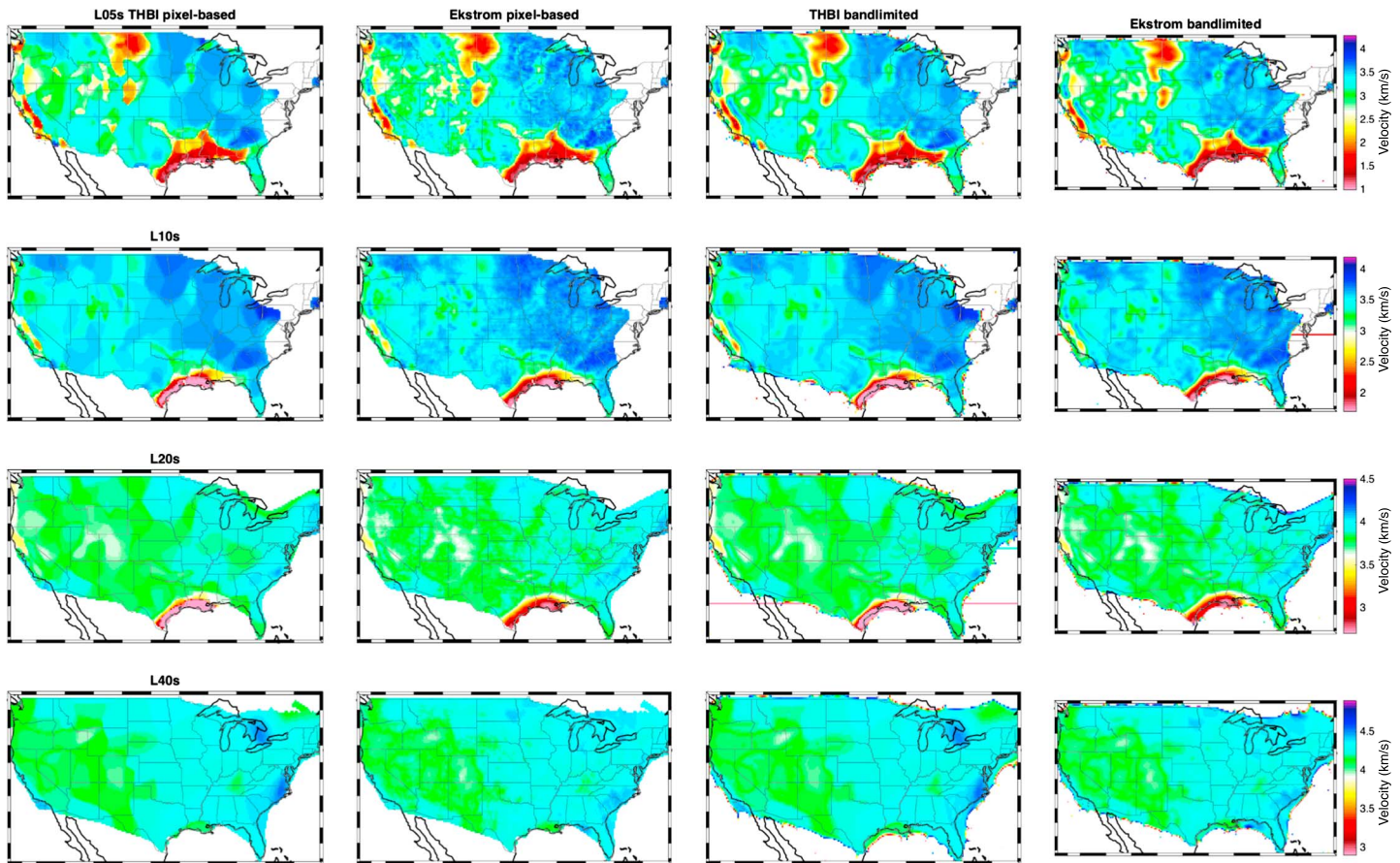
Figure 9. Phase velocity maps of Love waves for the THBI and *Ekström* model showing the (columns 1 and 2) pixel-based representation and (columns 3 and 4) filtered at a spherical harmonic cutoff of *l* = 200.

At shorter wavelengths (*l* > 120), the spectral amplitude is larger for the *Ekström* Rayleigh wave maps compared to that of the THBI (see Column 4 of Figure 8). This pattern seems reversed for Love waves (except for the longest period 40 s Love wave phase velocity map). Large spectral amplitude at shorter wavelengths (compared to longer wavelength, smaller spherical harmonic degrees) is due to the short-wavelength speckling observed in the *Ekström* phase velocity (and residual) maps, compared to the smoother THBI maps. On the other hand, the larger amplitude in the Love wave maps is related to the differences in length scale and amplitude of the small-scale low-velocity feature in the Mississippi embayment. The 40 s Love waves are less sensitive to this low-velocity feature and hence the spectra reverses to the general pattern of higher amplitudes for *Ekström* compared to THBI (see Column 4 of Figure 9, compare 40 s phase velocity maps with those from 5–20 s). At this period the spectral amplitudes are also more comparable.

4.6. Statistical Assessment of Crustal Models

The ambient noise phase velocity measurements can be used to invert for compressional and shear wave speed in the crust either by themselves [e.g., *Moschetti et al.*, 2007; *Bensen et al.*, 2008], or in combination with receiver functions [e.g., *Lowry and Pérez-Gussinyé*, 2011; *Shen et al.*, 2013]. In this paper, however, we use the statistical information to anticipate how these new data sets will inform the new models. We do this by comparing the observed THBI with the predicted phase velocity maps obtained using extensively used global (e.g., CRUST1.0 [*Laske et al.*, 2012] and LITHO1.0 [*Pasyanos et al.*, 2014]) and regional (e.g., NACr14 [*Tesauro et al.*, 2014]) crustal models in the U.S.

We calculate the predicted phase dispersion curves at each individual 1° × 1° tile in the three crustal models (similar resolution for CRUST1.0, LITHO1.0, and NACr14) using the propagator matrix method for computing dispersion curves in a layered isotropic elastic wave model [e.g., *Hisada*, 1994; *Lai and Rix*, 1998]. The
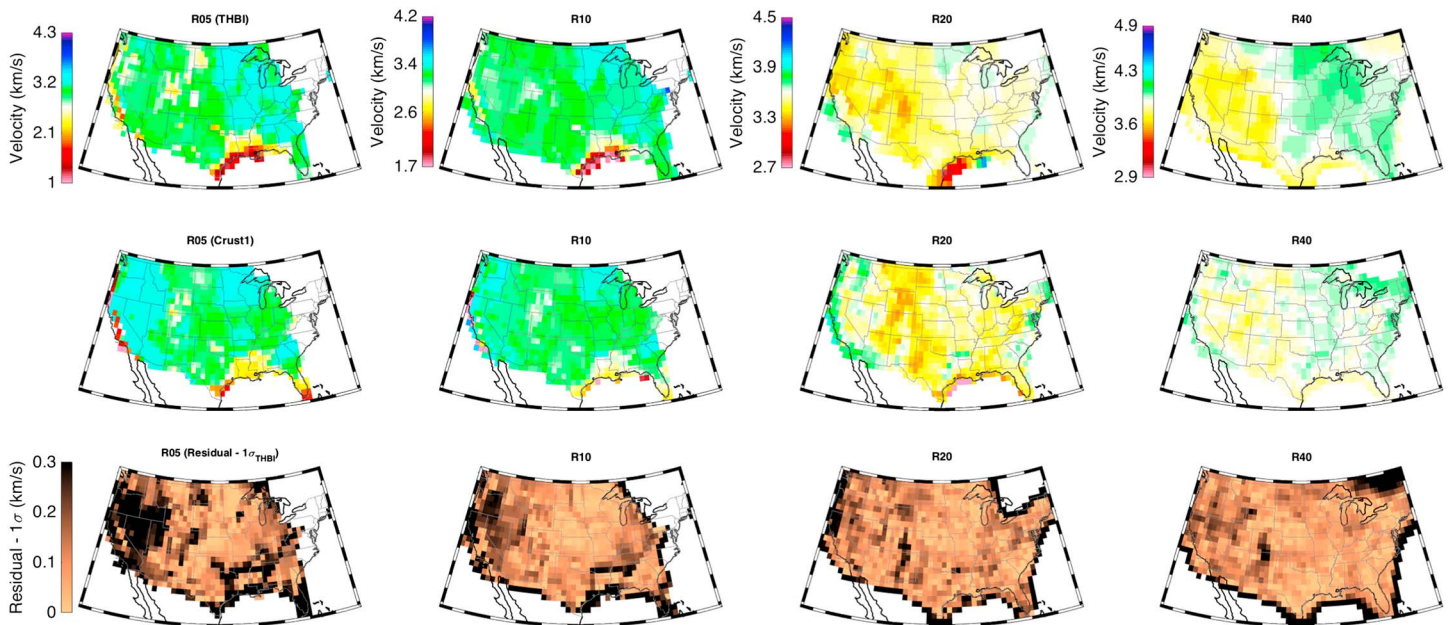
Figure 10. A statistical comparison between the observed (THBI) and predicted phase velocity maps (obtained from crustal models, CRUST1.0 see supporting information Figure S3, for comparison to LITHO1.0 and NACr14). (Row 1) The THBI phase velocity maps are resampled at the same resolution as the crustal models (e.g., 1° × 1° for CRUST1.0 and NACr14, respectively). (Row 2) Predicted phase velocity maps for Raleigh waves using CRUST1.0. (Row 3) The absolute residuals between the observed and predicted phase velocity maps, relative to the standard deviation of the THBI phase velocities (similar to Figure 4 but resampled at a resolution of 1° × 1°).

dispersion data are resampled at the frequencies of the predicted phase maps and are used to calculate residuals. The statistical significance of these residuals can be assessed by comparison with the THBI standard deviation at the same resolution (e.g., Figure 10 for CRUST1.0). For NACr14, which is only a compressional velocity model, we use the compressional to shear wave velocity and density scaling reported by *Brocher* [2005]. We conduct an analysis of the intraregional variation of the residuals based on the crustal classification scheme defined in *Mooney et al.* [1998] as well as the physiographic provinces [e.g., *Fenneman*, 1917] (see Figure 11a). We discuss these comparisons in the next section, paying special attention to the reasons for discrepancy across the various models and between model predictions and data.

5. Discussion

5.1. THBI Versus Least Squares: Damping, Smoothing, and Uncertainty

The phase velocity maps obtained using THBI agree well with those of the least squares approach especially at long wavelengths. The results from the residual maps and the multitaper spectral correlation analysis show that the few sources of dissimilarity come from two short-wavelength sources: (1) the very slow velocities in the sediment basins of southernmost Texas, Florida, and Mississippi, and (2) discretization and regularization artifacts mapped into the results from the least squares approach when a finely parameterized model is solved using damping and smoothing constraints that may not apply across the model domain (Figures 8 and 9). As pointed out earlier, the largest residuals are observed as short wavelength speckling that reduces with increasing period. Since the wavelength of velocity variation reduces at longer periods, applying a single smoothing and damping parameter is more justified than at shorter periods (see Figure 8). The THBI approach does not suffer from this limitation and is able to recover wavelengths of velocity variation of different sizes and smoothness (e.g., smooth and sharp velocity boundaries), without the need for explicit regularization (see for example 5 s phase velocity map in Figure 3).

5.2. Statistical Assessment of Crustal Models With Regionalization

Of the three crustal models we assess, only LITHO1.0 incorporates surface wave dispersion data derived from earthquake sources at longer periods, e.g., greater than 28 s (35 mHz) for Rayleigh and 30s
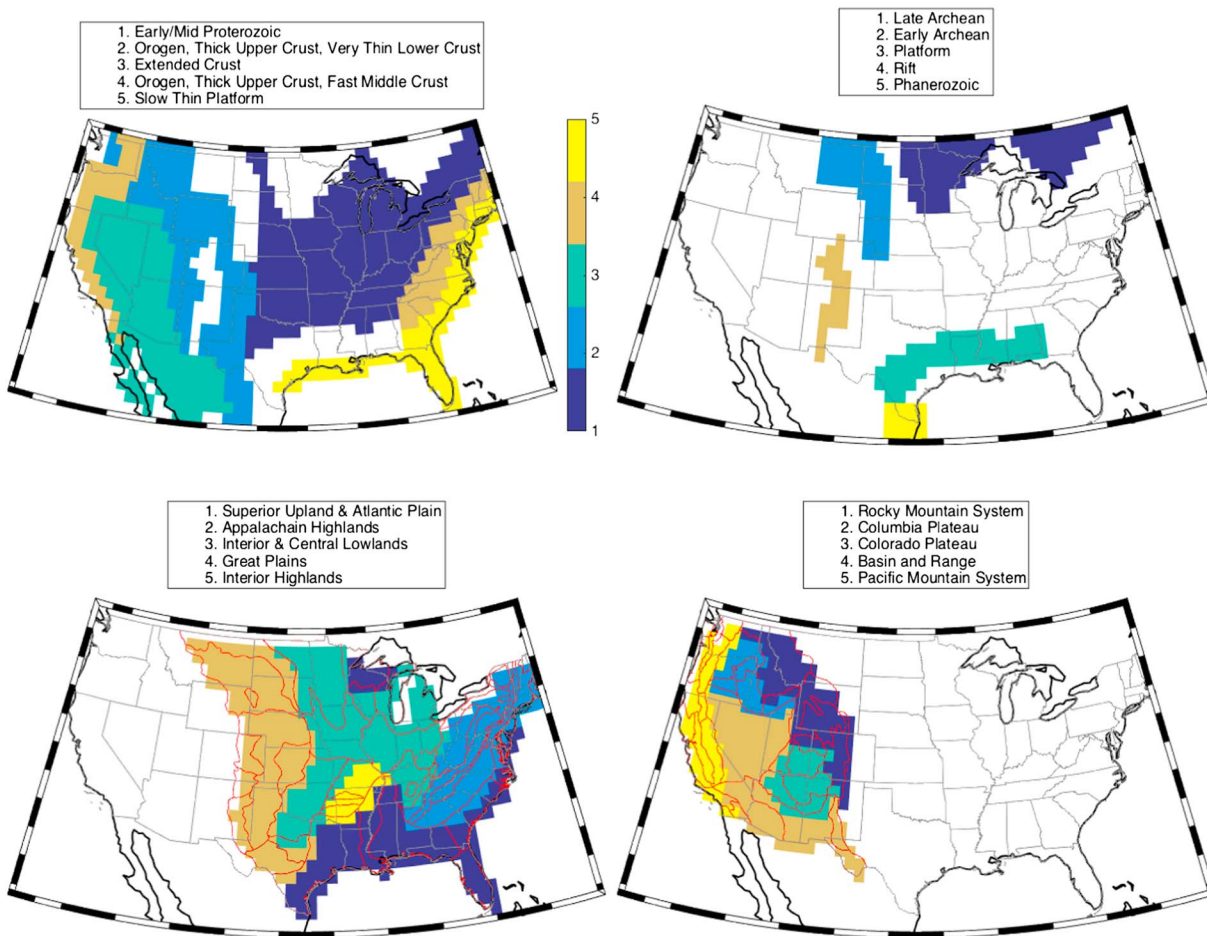
Figure 11a. Crustal classification schemes used in the assessment of Figure 11b. (Row 1) Crustal classification scheme based on crustal types in CRUST1.0 [e.g., *Mooney et al.*, 1998]. (Row 2) Crustal classification based on surface geology using the physiographic divisions described by *Fenneman* [1917].

(33 mHz) for Love [see *Pasyanos et al.*, 2014, Table 2]. The other crustal models, i.e., CRUST1.0 and NACr14, are derived primarily from active source data sets. Compared to CRUST1.0, NACr14 uses a larger active source database, although it only reports compressional wave velocities and does not include sedimentary layer structure. The crustal model of CRUST1.0 is synthesized from a template of 14 crustal types (using the tectonic regionalization Figure 11a of *Mooney et al.* [1998]). This approach allows the model to be extrapolated to regions where there are no data. When the residuals are sorted by this classification scheme, we observe statistically significant misfits between the observed and predicted phase dispersion data, except for the *Late Archean* region (see Figure 11b).

In all regions in the U.S., we observe the largest residuals at shorter periods (sedimentary basins or near surface structure), which decrease with increasing period for both Love and Rayleigh waves. A comparison of the residuals to the standard deviation maps derived from THBI shows that the differences are statistically significant at the 3σ level. The largest residuals are observed at the shortest periods for the Love waves, particularly in the regions called the *slow thin platforms* and the *Phanerozoic*. This is because the sensitivity of short-period Love waves is larger at the shallowest depths (<10 km, see Figures 12 and S4a–S4d) and is greater than that of Rayleigh waves, which, for the same period, tends to feel deeper structure. These differences are therefore attributable to the very slow Love and Rayleigh wave phase velocities in the sediment basins of the Mississippi embayment, which lead to residuals as large as 1.1 km/s in the southernmost regions of Texas, Florida and Mississippi. To illustrate how these residuals will reflect updates to the bulk crustal velocity structure, we show, as an example, a forward modeling exercise for a station in the extended crust, where updates to the shallow velocity structure significantly improve the short-period residuals (Figures 13 and S5). This analysis illustrates that
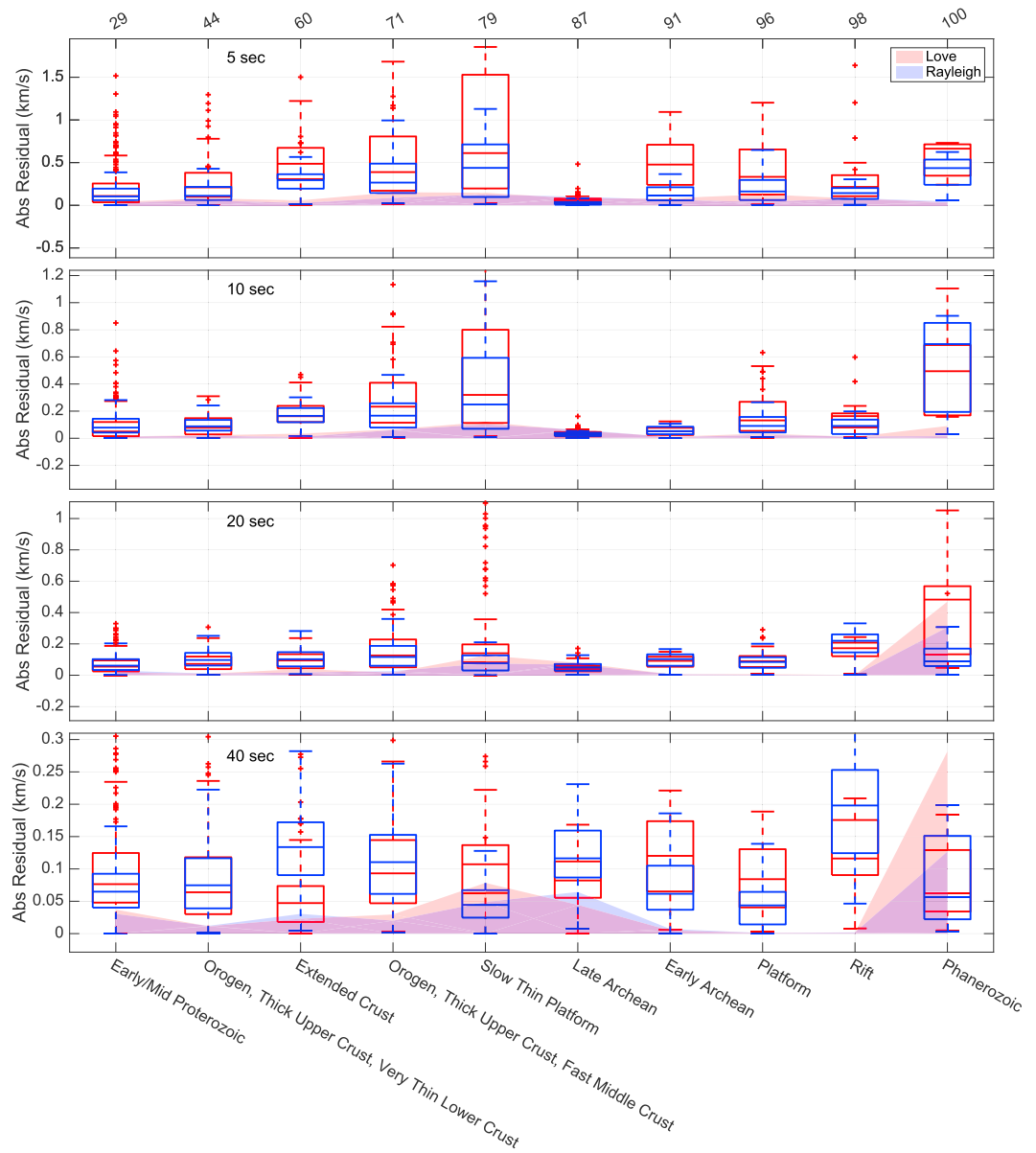
Figure 11b. Statistical assessment of CRUST1.0 within the USA compared to the observed data (derived from the residual and standard deviation maps of Figure 8). (Row 1) The average residual (box and whisker plots) for Love and Rayleigh waves within CRUST1.0 for each crustal type as defined in *Mooney et al.* [1998]. The crustal types are ordered from largest to smallest fractional area within the U.S. (numbers on top row from left to right on x axis). The boxplots show the lowest quartile, the median, and the third quartile. The shaded line plot shows the 3σ error from the standard deviation maps. The residuals are plotted for 5, 10, 20, and 40 s.

shallow velocity structure beneath sedimentary basins, especially in these regions, needs to be revisited. Additionally, a comparison of the residuals based on surface geology [e.g., *Fenneman*, 1917] shows a similar pattern to the crustal regionalization of *Mooney et al.* [1998]. In the regionalization based on surface geology, we observe larger intraregional variances, suggesting that the crustal regionalization scheme of *Mooney et al.* [1998] is preferred (compare supporting information Figures S1 to 11b).

As expected, LITHO1.0 shows a closer correspondence to the THBI results compared to both CRUST1.0 and NACr14, since it incorporates surface wave data at longer periods. On average, relative to THBI standard deviation, LITHO1.0 residual is 18% smaller than CRUST1.0 and 135% smaller than NACr14 (see Table 3). In all three models the residuals decrease with increasing period, with the minimum being reached at ~15 s
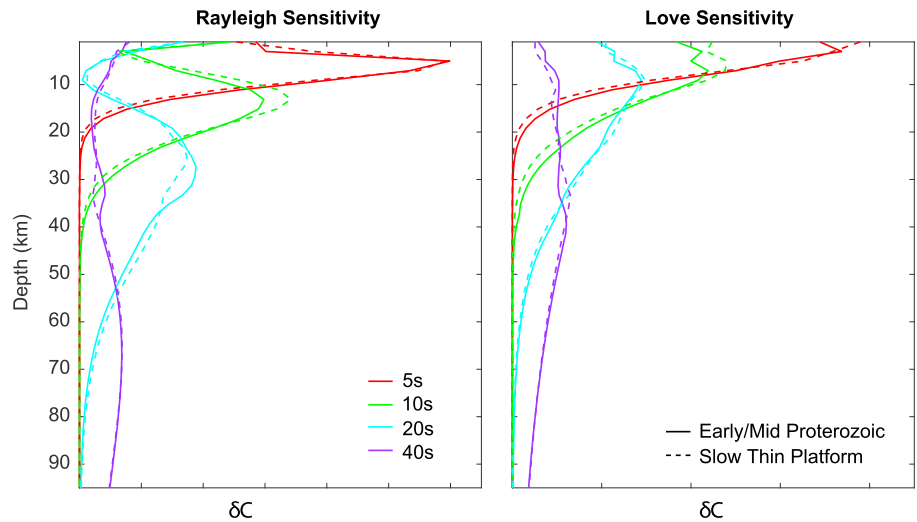
Figure 12. The depth sensitivity of Rayleigh and Love waves for the selection of periods shown in Figure 11b, using a representative regional crustal velocity model drawn from the average of all velocity profiles in the Early/Middle Proterozoic region (solid lines) and slow thin platforms (dashed lines) described in *Mooney et al.* [1998]. The change in phase velocity (*x* axis) is due to a 10% increase in density, V_p, and V_s at each depth (*y* axis).

(see supporting information Figure S2). The crustal structure in the region designated as *Late Archean* is well fit regardless of which model is used. Similarly, as evidenced by CRUST1.0, we observe the largest residuals in the *Phanerozoic* and *slow thin platform* domains of the crustal models of LITHO1.0 and NACr14. Compared to the other two models, the residuals derived from comparison with NACr14 are especially large due to the absence of sediment velocities in this published velocity model.

The most prominent features observed on our phase velocity maps are the very slow velocities that outline the sedimentary basins. A comparison of the boundaries of the major tectonic division of the Precambrian craton of North America [*Whitmeyer and Karlstrom*, 2007] and the dispersion maps (Figure 3) indicates the depths at which different tectonic regions are distinct from their surroundings. For example, while the
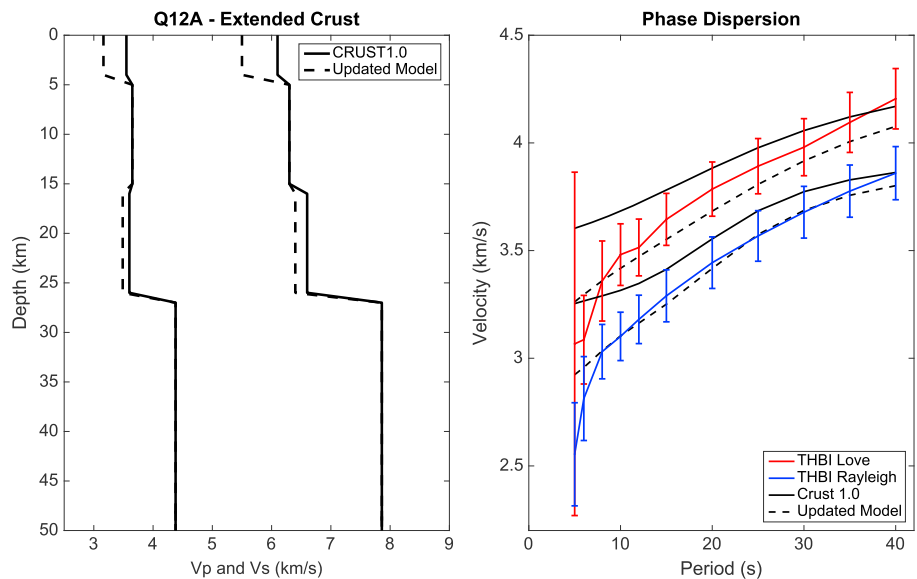
Figure 13. Forward modeling of phase dispersion curves at TA station Q12A on the extended crust region defined by *Mooney et al.* [1998]. (a) The CRUST1.0 velocity model (solid line) at this station is updated (dashed) line, to better fit the phase dispersion curves. (b) The observed THBI phase dispersion data with uncertainties (red for Love and blue for Rayleigh) compared to the predicted dispersion curves for the CRUST1.0 (solid line) and the updated model (dashed line).

Table 3. Data Coverage and Spatial Performance of the Different Crustal Models Based On THBI Statistics[a]

Region	LITHO1.0(L)	CRUST1.0(C)	NACR14 (N)	*LITHO Performance (C, N)
Early/Middle Proterozoic	3.4 [4.0, 2.8]	4.0 [4.1, 3.8]	6.3 [7.2, 5.4]	(17%, 85%)
Extended Crust	4.4 [4.3, 4.6]	5.0 [4.6, 5.5]	10.6 [9.9, 11.2]	(13%, 139%)
Orogen, Thick UC, and Thin LC	8.8 [7.2, 10.3]	7.9 [6.4, 9.3]	11.5 [9.4, 13.7]	(−10%, 32%)
Orogen, Thick UC, and Fast MC	2.9 [3.0, 2.8]	3.6 [3.6, 3.5]	4.2 [4.1, 4.3]	(22%, 44%)
Slow Thin Platform	3.0 [3.4, 2.8]	2.8 [3.2, 2.5]	5.3 [5.5, 5.1]	(−6%, 73%)
Late Archean	0.7 [0.9, 0.6]	0.8 [0.8, 0.7]	0.8 [0.9, 0.6]	(11%, 6%)
Early Archean	3.2 [4.1, 2.3]	5.4 [6.8, 4.1]	13.5 [15.6, 11.3]	(70%, 322%)
Platform	6.5 [5.8, 7.1]	6.5 [5.6, 7.5]	21.7 [15.4, 27.8]	(2%, 237%)
Rift	5.8 [4.0, 7.5]	10.1 [8.4, 11.9]	15.9 [13.8, 17.9]	(75%, 174%)
Phanerozoic	1.7 [1.6, 1.8]	1.5 [1.6, 1.5]	5.7 [5.9, 5.7]	(−11%, 237%)
			Average =	(18%, 135%)

[a]The numbers are averaged across all periods, for Love and Rayleigh waves, respectively. The overall average is then compared to LITHO1.0 values (*). Positive values represent better performance of LITHO1.0 and negative values, worse performance. $\bar{A}^{\bar{A}l,\bar{A}r}$ = Residual/THBI std. $\bar{A}$, $\bar{A}l$,$\bar{A}r$ (gross average, average Love, and Rayleigh, respectively).

boundaries of the Wyoming craton do not seem to systematically correspond to changes in phase velocities of the Love and Rayleigh waves at any period we analyze, the Superior craton does appear distinct (faster) from the Trans-Hudson orogeny to the west in the 10 and 20 s Love and Rayleigh maps.

By comparison, the largest low velocity feature in the Mississippi embayment marks the southernmost edge of the Precambrian basement, which experienced the detachment of a microcontinent. We also observe the distinct outlines of the Oklahoma aulacogen at periods of 5 and 10 s in both the Love and Rayleigh maps, indicating that the aulacogen is characterized by slower seismic wave speeds in the upper and midcrust than its surroundings. The Midcontinent Rift System is discernible in the 5 and 10 s Love and Rayleigh maps, particularly in Minnesota and Iowa, though its signature goes away at periods longer than 10 s (Figure 3). These slow velocity features, as well as the signature of the Williston (North Dakota) and Dever (Colorado) basins, are only visible at the shortest periods (particularly at 5 s) and gradually disappear at longer periods, suggesting that the updates to velocity structure are restricted to the upper crustal depths (see Figure 12). At longer periods (20 and 40 s), sensitive primarily to the middle-to-lower crust and sub-Moho mantle, most notable are large-scale velocity differences between the slower western and faster eastern United States, and slow regions along the northeastern and northwestern margins of the Colorado Plateau—corresponding to the High Rockies and the Wasatch Range—consistent with differences in lithospheric structure seen in scattered wave studies [e.g., *Lekić and Fischer*, 2014].

6. Conclusions

We present a new statistical data set of phase velocity maps and their associated uncertainties using a large Monte Carlo ensemble derived from a transdimensional hierarchical Bayesian inversion of a phase velocity dispersion data set for ambient noise surface waves. These maps are obtained using an autoadaptive model parameterization that does not require a priori assumptions on damping and smoothing, while constraining the level of observational and modeling uncertainties, which could otherwise affect model results. We show that observational uncertainties dominate and are strongly path dependent. We show, using pixel-based comparisons and multitaper spectral correlation analysis, that the maps obtained using the Bayesian inverse approach are comparable to those obtained using the linear least squares approach, with minor differences attributable to very slow velocities in the sedimentary basins of the southeastern U.S., and inversion artifacts from data-agnostic discretization or regularization using the linear least squares approach. We compare statistics derived from the Monte Carlo ensemble against predictions of three crustal models of the U.S. and organize the results based on regionalization. Favorable comparison is seen with the LITHO1.0 crustal model, which, not surprisingly, incorporates surface wave data at the longest periods. Based on the large discrepancy in-phase dispersion data for both Love and Rayleigh wave (except for *Late Archean* crust), we show that there is room for improvement across all models, especially for deriving new crustal regionalization schemes and for updating shallow velocity structure. We address these issues in a subsequent paper.

References

Aki, K. (1957), Space and time spectra of stationary stochastic waves, with special reference to microtremors, *Bull. Earthquake Res. Inst.*, *35*, 415–457, doi:http://hdl.handle.net/2261/11892.

Bassin, C., G. Laske, and G. Masters (2000), The current limits of resolution for surface wave tomography in North America, *Eos. Trans. AGU*, *81* F897.

Becker, T. W., and L. Boschi (2002), A comparison of tomographic and geodynamic mantle models, *Geochem., Geophys., Geosyst.*, *3*(1), 1003, doi:10.1029/2001GC000168.

Benoit, M. H., C. Ebinger, and M. Crampton (2014), Orogenic bending around a rigid Proterozoic magmatic rift beneath the Central Appalachian Mountains, *Earth Planet. Sci. Lett.*, *402*, 197–208, doi:10.1016/j.epsl.2014.03.064.

Bensen, G. D., M. H. Ritzwoller, M. P. Barmin, A. L. Levshin, F. Lin, M. P. Moschetti, N. M. Shapiro, and Y. Yang (2007), Processing seismic ambient noise data to obtain reliable broad-band surface wave dispersion measurements, *Geophys. J. Int.*, *169*(3), 1239–1260, doi:10.1111/j.1365-246X.2007.03374.x.

Bensen, G. D., M. H. Ritzwoller, and N. M. Shapiro (2008), Broadband ambient noise surface wave tomography across the United States, *J. Geophys. Res.*, *113*, B05306, doi:10.1029/2007JB005248.

Bensen, G. D., M. H. Ritzwoller, and Y. Yang (2009), A 3-D shear velocity model of the crust and uppermost mantle beneath the United States from ambient seismic noise, *Geophys. J. Int.*, *177*, 1177–1196, doi:10.1111/j.1365-246X.2009.04125.x.

Bodin, T., and M. Sambridge (2009), Seismic tomography with the reversible jump algorithm, *Geophys. J. Int.*, *178*(3), 1411–1436, doi:10.1111/j.1365-246X.2009.04226.x.

Bodin, T., M. Sambridge, H. Tkalčić, P. Arroucau, K. Gallagher, and N. Rawlinson (2012a), Transdimensional inversion of receiver functions and surface wave dispersion, *J. Geophys. Res.*, *117*, B02301, doi:10.1029/2011JB008560.

Bodin, T., M. Sambridge, N. Rawlinson, and P. Arroucau (2012b), Transdimensional tomography with unknown data noise, *Geophys. J. Int.*, *189*(3), 1536–1556, doi:10.1111/j.1365-246X.2012.05414.x.

Brocher, T. M. (2005), Empirical relations between elastic wavespeeds and density in the Earth's crust, *Bull. Seismol. Soc. Am.*, *95*(6), 2081–2092, doi:10.1785/0120050077.

Christensen, N. I., and W. D. Mooney (1995), Seismic velocity structure and composition of the continental crust: A global view, *J. Geophys. Res.*, *100*, 9761–9788, doi:10.1029/95JB00259.

Dahlen, F. A., and F. J. Simons (2007), Spectral estimation on a sphere in geophysics and cosmology, *Geophys. J. Int.*, *174*(3), 774–807, doi:10.1111/j.1365-246X.2008.03854.x.

Dalton, C. A., and J. B. Gaherty (2013), Seismic anisotropy in the continental crust of northwestern Canada, *Geophys. J. Int.*, *193*(1), 338–348, doi:10.1093/gji/ggs108.

Ekström, G. (2014), Love and Rayleigh phase-velocity maps, 5–40 s, of the western and central USA from USArray data, *Earth Planet. Sci. Lett.*, *402*, 42–49, doi:10.1016/j.epsl.2013.11.022.

Ekström, G., G. A. Abers, and S. C. Webb (2009), Determination of surface-wave phase velocities across USArray from noise and Aki's spectral formulation, *Geophys. Res. Lett.*, *36*, L18301, doi:10.1029/2009GL039131.

Fenneman, N. M. (1917), Physiographic subdivision of the United States, *Proc. Natl. Acad. Sci. U.S.A.*, *3*(1), 17, doi:10.1073/pnas.1207851.

Foster, A., M. Nettles, and G. Ekstrom (2014), Overtone interference in Array-based Love-wave phase measurements, *Bull. Seismol. Soc. Am.*, *104*(5), 2266–2277, doi:10.1785/0120140100.

Galetti, E., A. Curtis, G. A. Meles, and B. Baptie (2015), Uncertainty loops in travel-time tomography from nonlinear wave physics, *Phys. Rev. Lett.*, *114*(14), 148501, doi:10.1103/PhysRevLett.114.148501.

Green, P. (1995), Reversible jump Markov chain Monte Carlo computation and Bayesian model determination, *Biometrika*, *82*(4), 711–732, doi:10.1093/biomet/82.4.711.

Green, P. J. (2003), Trans-dimensional Markov chain Monte Carlo, in *Highly Structured Stochastic Systems*, vol. 27, edited by P. J. Green, N. L. Hjort, and S. Richardson, pp. 179–198, Oxford Univ. Press, New York.

Hans Wedepohl, K. (1995), The composition of the continental crust, *Geochim. Cosmochim. Acta*, *59*(7), 1217–1232, doi:10.1016/0016-7037(95)00038-2.

Harig, C., K. W. Lewis, A. Plattner, and F. J. Simons (2015), A suite of software analyzes data on the sphere, *Eos (Washington. DC)*, *96*, 1–10, doi:10.1029/2015EO025851.

Hisada, Y. (1994), An efficient numerical method for computing synthetic seismograms for a layered half-space with sources and receivers at close or same depths, *Bull. Seismol. Soc. Am.*, *84*(5), 1456–1472, doi:10.1007/PL00012546.

Hopper, E., K. M. Fischer, L. S. Wagner, and R. B. Hawman (2017), Reconstructing the end of the Appalachian orogeny, *Geology*, *45*(1), 15–18, doi:10.1130/G38453.1.

Huang, Y., V. Chubakov, F. Mantovani, R. L. Rudnick, and W. F. McDonough (2013), A reference Earth model for the heat-producing elements and associated geoneutrino flux, *Geochem., Geophys., Geosyst.*, *14*, 2003–2029, doi:10.1002/ggge.20129.

Lai, C. G., and G. J. Rix (1998), Simultaneous inversion of Rayleigh phase velocity and attenuation for near-surface site characterization, School of Civ. and Environ. Eng., Ga. Inst. of Technol.

Laske, G., G. Masters, Z. Ma, and M. E. Pasyanos (2012), CRUST 1.0: An updated global model of the Earth's Crust, *EGU Meet. Abstr.*, (EGU2012-3743).

Lekić, V., and K. M. Fischer (2014), Contrasting lithospheric signatures across the western United States revealed by Sp receiver functions, *Earth Planet. Sci. Lett.*, *402*, 90–98, doi:10.1016/j.epsl.2013.11.026.

Liang, C., and C. A. Langston (2008), Ambient seismic noise tomography and structure of eastern North America, *J. Geophys. Res.*, *113*, B03309, doi:10.1029/2007JB005350.

Lin, F., and B. Schmandt (2014), Upper crustal azimuthal anisotropy across the contiguous US determined by Rayleigh wave ellipticity, *Geophys. Res. Lett.*, *41*, 8301–8307, doi:10.1002/2014GL062362.

Long, M. D., A. Levander, and P. M. Shearer (2014), An introduction to the special issue of Earth and Planetary Science Letters on USArray science, *Earth Planet. Sci. Lett.*, *402*, 1–5, doi:10.1016/j.epsl.2014.06.016.

Lowry, A. R., and M. Pérez-Gussinyé (2011), The role of crustal quartz in controlling Cordilleran deformation, *Nature*, *471*(7338), 353–357, doi:10.1038/nature09912.

Malinverno, A., and V. A. Briggs (2004), Expanded uncertainty quantification in inverse problems: Hierarchical Bayes and empirical Bayes, *Geophysics*, *69*(4), 1005–1016, doi:10.1190/1.1778243.

Malinverno, A., and R. L. Parker (2006), Two ways to quantify uncertainty in geophysical inverse problems, *Geophysics*, *71*(3), W15–W27, doi:10.1190/1.2194516.

Menke, W. (2012), Solution of the linear, Gaussian inverse problem, viewpoint 3, in *Geophysical Data Analysis: Discrete Inverse Theory*, pp. 89–114, Elsevier, doi:10.1016/B978-0-12-397160-9.00018-7.

Menke, W., and G. Jin (2015), Waveform fitting of cross spectra to determine phase velocity using Aki's formula, *Bull. Seismol. Soc. Am.*, *105*(3), 1–9, doi:10.1785/0120140245.

Meschede, M., and B. Romanowicz (2015), Lateral heterogeneity scales in regional and global upper mantle shear velocity models, *Geophys. J. Int.*, *200*, 1076–1093, doi:10.1093/gji/ggu424.

Mooney, W. D., G. Laske, and T. G. Masters (1998), CRUST 5.1: A global crustal model at 5° × 5°, *J. Geophys. Res.*, *103*(B1), 727–747, doi:10.1029/97JB02122.

Moschetti, M. P., M. H. Ritzwoller, and N. M. Shapiro (2007), Surface wave tomography of the western United States from ambient seismic noise: Rayleigh wave group velocity maps, *Geochem., Geophys., Geosyst.*, *8*, Q08010, doi:10.1029/2007GC001655.

Moschetti, M. P., M. H. Ritzwoller, F.-C. Lin, and Y. Yang (2010a), Crustal shear wave velocity structure of the western United States inferred from ambient seismic noise and earthquake data, *J. Geophys. Res.*, *115*, B10306, doi:10.1029/2010JB007448.

Moschetti, M. P., M. H. Ritzwoller, F. Lin, and Y. Yang (2010b), Seismic evidence for widespread western-US deep-crustal deformation caused by extension, *Nature*, *464*(7290), 885–889, doi:10.1038/nature08951.

Nataf, H.-C., and Y. Ricard (1996), 3SMAC: An a priori tomographic model of the upper mantle based on geophysical modeling, *Phys. Earth Planet. Inter.*, *95*(1–2), 101–122, doi:10.1016/0031-9201(95)03105-7.

Pasyanos, M. E., T. G. Masters, G. Laske, and Z. Ma (2014), LITHO1.0: An updated crust and lithospheric model of the Earth, *J. Geophys. Res. Solid Earth*, *119*, 2153–2173, doi:10.1002/2013JB010626.

Pollitz, F. F., and W. D. Mooney (2014), Seismic structure of the Central US crust and shallow upper mantle: Uniqueness of the Reelfoot Rift, *Earth Planet. Sci. Lett.*, *402*(C), 157–166, doi:10.1016/j.epsl.2013.05.042.

Prieto, G. A., J. F. Lawrence, and G. C. Beroza (2009), Anelastic Earth structure from the coherency of the ambient seismic field, *J. Geophys. Res.*, *114*, B07303, doi:10.1029/2008JB006067.

Ray, A., D. L. Alumbaugh, G. M. Hoversten, and K. Key (2013), Robust and accelerated Bayesian inversion of marine controlled-source electromagnetic data using parallel tempering, *Geophysics*, *78*(6), E271–E280, doi:10.1190/geo2013-0128.1.

Rudnick, R. L., and S. Gao (2014), Composition of the continental crust, in *Treatise on Geochemistry*, vol. 4, pp. 1–51, Elsevier, San Diego, Calif.

Sambridge, M., J. Braun, and H. McQueen (1995), Geophysical parametrization and interpolation of irregular data using natural neighbours, *Geophys. J. Int.*, *122*(3), 837–857, doi:10.1111/j.1365-246X.1995.tb06841.x.

Sambridge, M., K. Gallagher, A. Jackson, and P. Rickwood (2006), Trans-dimensional inverse problems, model comparison and the evidence, *Geophys. J. Int.*, *167*(2), 528–542, doi:10.1111/j.1365-246X.2006.03155.x.

Sambridge, M., T. Bodin, K. Gallagher, and H. Tkalcic (2012), Transdimensional inference in the geosciences, *Philos. Trans. R. Soc. A Math. Phys. Eng. Sci.*, *371*(1984), 201105474, doi:10.1098/rsta.2011.0547.

Saygin, E., P. R. Cummins, A. Cipta, R. Hawkins, R. Pandhu, J. Murjaya, Masturyono, M. Irsyam, S. Widiyantoro, and B. L. N. Kennett (2016), Imaging architecture of the Jakarta Basin, Indonesia with transdimensional inversion of seismic noise, *Geophys. J. Int.*, *204*(2), 918–931, doi:10.1093/gji/ggv466.

Schmandt, B., F. Lin, and K. E. Karlstrom (2015), Distinct crustal isostasy trends east and west of the Rocky Mountain front, *Geophys. Res. Lett.*, *42*, 10,290–10,298, doi:10.1002/2015GL066593.

Shapiro, N. M. (2005), High-resolution surface-wave tomography from ambient seismic noise, *Science*, *307*(5715), 1615–1618, doi:10.1126/science.1108339.

Shen, W., and M. H. Ritzwoller (2016), Crustal and uppermost mantle structure beneath the United States, *J. Geophys. Res. Solid Earth*, *121*, 4306–4342, doi:10.1002/2016JB012887.

Shen, W., M. H. Ritzwoller, and V. Schulte-Pelkum (2013), A 3-D model of the crust and uppermost mantle beneath the central and western US by joint inversion of receiver functions and surface wave dispersion, *J. Geophys. Res. Solid Earth*, *118*, 262–276, doi:10.1029/2012JB009602.

Simons, F. J., F. A. Dahlen, and M. A. Wieczorek (2006), Spatiospectral concentration on a sphere, *SIAM Rev.*, *48*(3), 504–536, doi:10.1137/S0036144504445765.

Stachnik, J. C., K. Dueker, D. L. Schutt, and H. Yuan (2008), Imaging Yellowstone plume-lithosphere interactions from inversion of ballistic and diffusive Rayleigh wave dispersion and crustal thickness data, *Geochem., Geophys., Geosyst.*, *9*, Q06004, doi:10.1029/2008GC001992.

Tesauro, M., M. K. Kaban, W. D. Mooney, and S. Cloetingh (2014), NACr14: A 3D model for the crustal structure of the North American Continent, *Tectonophysics*, *631*, 65–86, doi:10.1016/j.tecto.2014.04.016.

Tsai, V. C., and M. P. Moschetti (2010), An explicit relationship between time-domain noise correlation and spatial autocorrelation (SPAC) results, *Geophys. J. Int.*, *182*(1), 454–460, doi:10.1111/j.1365-246X.2010.04633.x.

Whitmeyer, S. J., and K. E. Karlstrom (2007), Tectonic model for the Proterozoic growth of North America, *Geosphere*, *3*(4), 220–259, doi:10.1130/GES00055.1.

Yang, Y., M. H. Ritzwoller, F. C. Lin, M. P. Moschetti, and N. M. Shapiro (2008), Structure of the crust and uppermost mantle beneath the western United States revealed by ambient noise and earthquake tomography, *J. Geophys. Res.*, *113*, B12310, doi:10.1029/2008JB005833.

Yang, Y., M. H. Ritzwoller, and C. H. Jones (2011), Crustal structure determined from ambient noise tomography near the magmatic centers of the Coso region, southeastern California, *Geochem., Geophys., Geosyst.*, *12*, Q02009, doi:10.1029/2010GC003362.

Young, M., N. Rawlinson, and T. Bodin (2013), Transdimensional inversion of ambient seismic noise for 3D shear velocity structure of the Tasmanian crust, *Geophysics*, *78*(3), WB49–WB62, doi:10.1190/geo2012-0356.1.

Yuan, H. (2015), Secular change in Archaean crust formation recorded in Western Australia, *Nat. Geosci.*, *8*(10), 808–813, doi:10.1038/ngeo2521.

Zhang, H., et al. (2016), Distinct crustal structure of the North American midcontinent rift from *P* wave receiver functions, *J. Geophys. Res. Solid Earth*, *121*, 8136–8153, doi:10.1002/2016JB013244.